Suspended Sediments in Chilean Rivers Reveal Low Postseismic Erosion After the Maule Earthquake (Mw 8.8) During a Severe Drought

Violeta Tolorza, C. H. Mohr, S. Carretier, A. Serey, S. A. Sepúlveda, J. Tapia, L. Pinto

JGR Earth Surface

RESEARCH ARTICLE
10.1029/2018JF004766

Suspended Sediments in Chilean Rivers Reveal Low Postseismic Erosion After the Maule Earthquake (Mw 8.8) During a Severe Drought

Violeta Tolorza[1], C. H. Mohr[2], S. Carretier[3], A. Serey[4], S. A. Sepúlveda[4,5], J. Tapia[6], and L. Pinto[4]

[1]Instituto de Ciencias de la Tierra, Universidad Austral de Chile, Campus Isla Teja, Valdivia, Chile, [2]Institute of Environmental Sciences and Geography, University of Potsdam, Potsdam, Germany, [3]Géosciences Environnement Toulouse, IRD, OMP, UPS, CNRS, Université de Toulouse, Toulouse, France, [4]Departamento de Geología, Universidad de Chile, Santiago, Chile, [5]Instituto de Ciencias de la Ingeniería, Universidad de O´Higgins, Rancagua, Chile, [6]Escuela de Geología, Universidad Santo Tomás, Santiago, Chile

Key Points:
- Postseismic suspended sediment fluxes decreased during moderate- to high-flow conditions with respect to background values
- A reduced hillslope-channel connectivity due to drought and limited coseismic landsliding set the catchment-wide erosive response
- During postseismic dry conditions, the first-order control on catchment-wide erosion is the combined effect of topography and land cover

Supporting Information:
- Supporting Information S1
- Table S1
- Table S2
- Table S3
- Table S4
- Data Set S1
- Data Set S2
- Data Set S3
- Data Set S4

Correspondence to:
V. Tolorza,
violeta.tolorza@uach.cl

Citation:
Tolorza, V., Mohr, C. H., Carretier, S., Serey, A., Sepúlveda, S. A., Tapia, J., & Pinto, L. (2019). Suspended sediments in Chilean rivers reveal low postseismic erosion after the Maule earthquake (Mw 8.8) during a severe drought. *Journal of Geophysical Research: Earth Surface*, *124*, 1378–1397. https://doi.org/10.1029/2018JF004766

Received 22 MAY 2018
Accepted 17 APR 2019
Accepted article online 25 APR 2019
Published online 5 JUN 2019

Abstract We address the question of whether all large-magnitude earthquakes produce an erosion peak in the subaerial components of fluvial catchments. We evaluate the sediment flux response to the Maule earthquake in the Chilean Andes (Mw 8.8) using daily suspended sediment records from 31 river gauges. The catchments cover drainage areas of 350 to around 10,000 km^2, including a wide range of topographic slopes and vegetation cover of the Andean western flank. We compare the 3- to 8-year postseismic record of sediment flux to each of the following preseismic periods: (1) all preseismic data, (2) a 3-year period prior to the seismic event, and (3) the driest preseismic periods, as drought conditions prevailed in the postseismic period. Following the earthquake, no increases in suspended sediment flux were observed for moderate to high percentiles of the streamflow distribution (mean, median, and ≥75th percentile). However, more than half of the examined stations showed increased sediment flux during baseflow. By using a Random Forest approach, we evaluate the contributions of seismic intensities, peak ground accelerations, co-seismic landslides, hydroclimatic conditions, topography, lithology, and land cover to explain the observed changes in suspended sediment concentration and fluxes. We find that the best predictors are hillslope gradient, low-vegetation cover, and changes in streamflow discharge. This finding suggests a combined first-order control of topography, land cover, and hydrology on the catchment-wide erosion response. We infer a reduced sediment connectivity due to the postseismic drought, which increased the residence time of sediment detached and remobilized following the Maule earthquake.

1. Introduction

Earthquakes shape topography by coseismic uplift and simultaneously reduce relief by enhancing erosion. These processes define the role of large earthquakes in terms of the mass balance of mountain belts (Hovius et al., 2011; Li et al., 2014). A better understanding of the processes triggered by high-magnitude earthquakes helps to constrain this long-term trade-off between uplift and erosion. In addition, the observation and description of such large-scale disturbances triggered by earthquakes are relevant for improving our knowledge regarding hazard and risk assessment associated with catastrophic events.

Earthquakes disturb the surface of the Earth and potentially modify sediment transfers from sources to sinks. Regarding sediment sources, a direct relation has been proposed between earthquake magnitude and the total area and volume of coseismic mass wasting in epicentral areas (Keefer, 1994; Malamud et al., 2004; Marc et al., 2017; Rodríguez et al., 1999). The propensity for failure after shallow earthquakes increases the rate of landslides during the first 1–4 years after the earthquake, which may also be controlled by earthquake magnitude (Marc et al., 2015). However, the erosive efficacy of large earthquakes also likely depends on site-specific topography (Meunier et al., 2008; Sepúlveda et al., 2005, 2010), glacial cover (Gorum et al., 2014), and fault type and depth (e.g., Antinao & Gosse, 2009; Gorum et al., 2014). From the available catalogs of landslides from recent shallow earthquakes, Marc et al. (2016) proposed a predictive model to estimate the total volume mobilized by landslides attributable to earthquakes. This model considers parameters describing the earthquake properties and landscape. However, it was not designed for subduction earthquakes, which represent end-members in terms of earthquake magnitude, but with

limited onshore ground motion that restricts the number and overall volume of coseismic landslides (Lacroix et al., 2013).

Regarding sediment transfer by rivers, sediment yields triggered by earthquakes are among the highest reported (Korup, 2012). Landslides induced by earthquakes provide fine-grained sediment supplies (e.g., Wang et al., 2015), which may increase the concentration of sediment in rivers independent of the variability of storms (Dadson et al., 2004; Hovius et al., 2011). Nonetheless, the residence time of the detached sediment may last from years to centuries and is inversely proportional to the frequency of intense runoff events (Wang et al., 2015). This observation highlights the fact that the catchment-wide erosion response is sensitive not only to landsliding but also to the establishment of connectivity that is needed for routing sediments to, and through, rivers (e.g., Fryirs, 2013). Hillslope-channel connectivity is established through discontinuous surface runoff, which depends on climate and site-specific thresholds for rainfall intensity. Sediment routing through rivers may also be modified by earthquakes. For example, landslides induced by earthquakes can dam rivers and modify drainage networks (Korup, 2005), as was the case for the Riñihuaso event following the 1960 Mw 9.5 Valdivia megathrust earthquake (Araya et al., 2014; Davis & Karzulovíc, 1963). Seismic shaking also triggers hydrological responses (Manga & Wang, 2015), disturbing streamflow at a regional to continental scale (e.g., Mohr et al., 2017; Montgomery & Manga, 2003; Shi et al., 2015). Given that seismic events can increase streamflow by up to a factor of five compared to preseismic conditions (Mohr et al., 2017), these streamflow pulses may plausibly be relevant for the transport of sediment at the landscape-scale.

Large earthquakes, including megathrusts, are well recorded in the stratigraphy of lacustrine sediments (Howarth et al., 2012; Moernaut et al., 2015, 2018). In southern Chile, lacustrine turbidites sourced from hemipelagic sediments are generated over a macroseismic intensity threshold of VI ½ to VII ½ (Moernaut et al., 2018). Earthquakes may also trigger lake tsunamis, subaquatic landslides, and delta collapses. These disturbances, together with the sediment sourced from subaerial coseismic landslides, generate differentiable deposits in the lacustrine stratigraphy (Van Daele et al., 2015).

Along the western flank of the Peruvian segment of the Central Andes, the cumulative seismic moment is greatest along the subduction interface and is thus below the coastline. This region does not coincide with the catchments yielding the highest decennial suspended sediments, which instead are located further inland, close to the main water divide (Morera et al., 2017). This observation, together with the restricted volume of coseismic landslides observed in a recent Andean megathrust earthquake (Lacroix et al., 2013), suggests a low catchment-wide erosional response to this type of seismic event. In this context, studying the net effect of a large megathrust on sediment fluxes may help to test if interplate megathrusts produce a postseismic erosion peak, as is the case for relatively shallow, large (Mw $\geq$ 7.3), intraplate earthquakes (Dadson et al., 2004; Hovius et al., 2011; Wang et al., 2015). Studying an individual megathrust may also allow exploration of whether the postseismic sediment fluxes are dominated by the volume of co-seismic landsliding (supply limited) or by surface runoff and its effect on hillslope-channel connectivity (transport limited).

The Maule earthquake (Mw 8.8) occurred in the Chilean segment of the Central Andes, involving a rupture zone of around 500 $\times$ 140 km (Figure 1a). This event is the second largest in magnitude recorded in the Andean subduction margin and is the fifth largest worldwide (ANSS Comprehensive Earthquake Catalog, https://earthquake.usgs.gov/data/comcat/, 09/26/2018). Despite the relatively low number of coseismic landslides triggered by this megathrust (Figure S1 in the supporting information; Serey et al., 2019) compared to earthquakes in other regions of the world (section 3), the Maule earthquake produced the largest reported coseismic release of water by rivers (Mohr et al., 2017) and triggered widespread turbidite deposits in the lakes of south-central Chile (Van Daele et al., 2015). Here, we examine the above questions of whether interplate megathrusts produce post-seismic erosion peaks and whether the post-seismic fluxes are dominated by the supply of landslide material or by surface runoff and consequent hillslope-channel connectivity (i.e., supply- vs. transport-limited response). To address these questions, we take advantage of the large number of monitored streams in this part of Chile to document the changes of suspended sediment fluxes in rivers before and after the Maule earthquake. We relate the observed response to a variety of factors, including local seismic effects (coseismic landslides, seismic intensities, and peak ground accelerations [PGAs]), hydroclimate, topography, lithology, and land cover for the studied catchments.

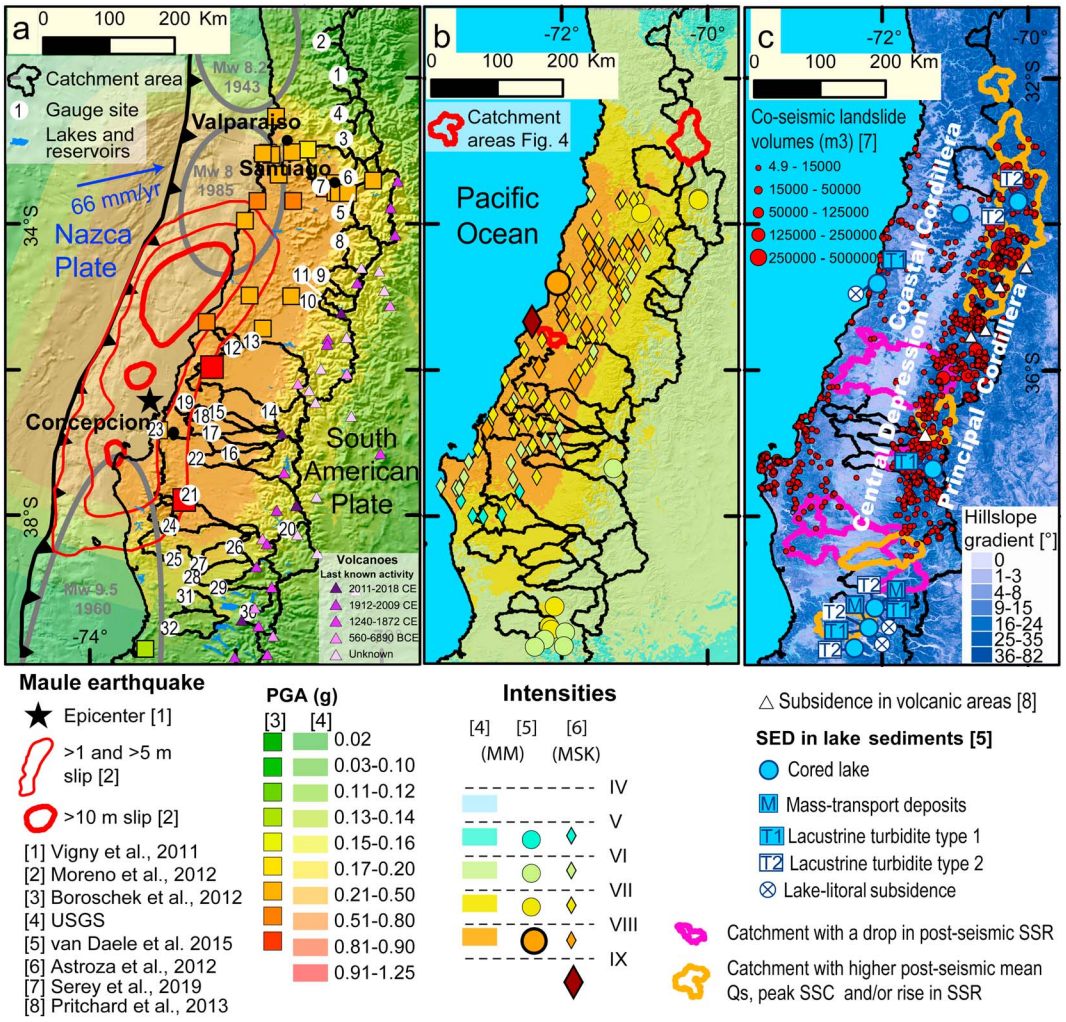

Figure 1. Location and setting of the Maule earthquake. (a) Horizontal peak ground accelerations and (b) seismic intensities in relation to the hydrometric stations and their drainage areas. Background colors represent modeled values from the U.S. Geological Survey. Point data are from Boroschek et al. (2012), Van Daele et al. (2015), and Astroza et al. (2012). Gray ellipses in (a) indicate the approximate extent of large (Mw≥8) megathrust events in the 100 years preceding the Maule earthquake (Campos et al., 2002; Lin et al., 2013). (c) Main disturbances triggered by the earthquake: coseismic subaerial landslides (Serey et al., 2019), seismically induced event deposits (SED; Van Daele et al., 2015) and volcanic areas with coseismic subsidence (Pritchard et al., 2013). The catchments outlined in yellow present some of the following responses: higher mean values of suspended sediment fluxes with respect to one or more of the background preseismic periods, historical maximum suspended sediment concentrations, and/or rise in the sediment rating curves during the postseismic period. Catchments with a drop in the postseismic sediment rating curve are outlined in pink. Background topographic models were obtained from (a) the GEBCO_2014 Grid, version 20150318, http://www.gebco.net, and (b and c) a merged digital elevation model (DEM; Shuttle Radar Topography Mission [SRTM] 1 arc-second —TanDEM-X ©DLR 2017 re-sampled to 30 m).

2. Study Region

Our study area is part of the continental Andean western flank (~32-40°S), where two longitudinal ranges (the Coastal Cordillera and the Principal Cordillera) are separated by a piedmont region, the Central Depression (Figure 1). The active volcanic arc is located in the Principal Cordillera, and this range also comprises extensive and thicker Cenozoic volcanic and clastic units. Hard rocks and steep slopes are present in both ranges, but the Coastal Cordillera in Central Chile has lower modal slopes (Figure S2), lacks deposits from recent and ancient volcanic activity, and hosts a larger proportion of metamorphic and intrusive rocks compared to the Principal Cordillera (Figure S3).

Neogene tectonic deformation in the study area has both longitudinal and latitudinal spatial variations (Charrier et al., 2007; Tapia et al., 2015). An acceleration of exhumation was documented at 10 to 2 Ma (Farías et al., 2008; Maksaev et al., 2009), but between 35 and 38°S, low-temperature thermochronology shows a wide range of ages between 20 and 6 Ma (Spikings et al., 2008). The interplay between the tectonic history and the climate pattern has led to millennial and decennial erosion rates decreasing southward, mainly correlated with decreasing mean slope, and increasing vegetation and rainfall (Carretier et al., 2013).

The cycle of subduction-zone seismicity in Chile exhibits both long seismic gaps (over decades to centuries) and earthquakes occurring in rapid succession (over hours to years) in nearby fault segments (e.g., Melnick et al., 2017). As a result, the entire study area was affected at least once by a large (Mw≥8) megathrust event in the past century (Figure 1a; Lin et al., 2013). Thus, we assume that, in general, hillslopes have been recently disturbed by megathrusts along the entire study area, yet the more southern regions suffered the highest seismic impact owing to the Valdivia (Mw 9.5) and Maule (Mw 8.8) earthquakes.

Longitudinally, the climate transitions from a Mediterranean to a temperate climate at ~38°S, with an increase in annual rainfall from ~250 to >2,000 mm to the south. In the Mediterranean segment, the annual precipitation is concentrated during the Austral Winter (June–August). During the Austral Summer (December–February), the Principal Cordillera is affected by convective rainfall. North of 36°S, these heavy rainfall events contribute to less than 10% of the annual precipitation. However, rainfall during these events may occur above 4,000 m above sea level, where snow cover is commonly present (Viale & Garreaud, 2014). These storm events are considered as main triggers of mass wasting, such as the rainfall produced by the 2013 summer storms (Sepúlveda et al., 2015). The strong interannual precipitation variability is modulated by the El Niño Southern Oscillation (ENSO; Aceituno, 1988) and its seasonal expressions (Montecinos & Aceituno, 2003). Nonetheless, the longest lasting (>6 years) and spatially extraordinarily large (30–38°S) drought affecting central Chile, which started in 2010, was decoupled from the negative ENSO phase. Judging from the past (Garreaud et al., 2017), negative ENSO phases commonly accompany drought. This most recent drought event is considered a megadrought based on hydrometric and dendrochronological data, resulting in a sharp decline in river discharge of up to 90% (Garreaud et al., 2017).

3. The Maule Earthquake

The Mw 8.8 Maule earthquake (27 February 2010) nucleated and propagated along the convergent Nazca-South American plate boundary (Figure 1a). It had a duration of ~2.5 min, reaching a slip of up to ~16 and 10 m in the northern and southern rupture segments, respectively (Moreno et al., 2012). The rupture zone extended horizontally for ~500 × 140 km and vertically in depth to ~5–45 km (Vigny et al., 2011). Corrected local PGA records reached up to 0.93 g in the horizontal component and 0.7 g in the vertical component (Boroschek et al., 2012). In addition, one station recorded 1.25 g before saturation (Saragoni & Ruiz, 2012). The U.S. Geological Survey (USGS) PGA interpolation had systematically lower values than the local records (Figure 1a), which may be due to site effects at the local seismic stations (Boroschek et al., 2012). Twenty-one percent of the MSK-64 intensities exceeded VII (Astroza et al., 2012), and only one value reached the maximum of IX in the coastal town of Constitución (Figure 1b). Although higher slip occurred under the ocean, the entire continental forearc region suffered MM intensities that exceeded V (U.S. Geological Survey [USGS], 2010) and VII in specific locations (Van Daele et al., 2015; Figure 1b).

The largest aftershock occurred on 2 January 2011 and was characterized by a Mw of 7.2, a focal depth of 24 km, and PGA values between 0.08 and 0.32 g. Two seismic events with normal focal mechanisms (Mw 6.9 and 7) occurred on 11 March 2010 and PGA values at that time reached up to 0.24 g (https://earthquake.usgs.gov/earthquakes/eventpage/usp000h94v/shakemap/pga, 10/14/18). These events began a seismic sequence with Mw>4 at a depth of 10–25 km (Farías et al., 2011).

Topographic effects of the Maule earthquake include coseismic uplift (up to +2.5 m) and subsidence (up to -1 m) in the coastal region (Farías et al., 2010). In addition, local subsidence of lakes (Van Daele et al., 2015) and up to 15 m of subsidence in volcanic areas occurred in the Principal Cordillera (Pritchard et al., 2013; Figure 1c). The earthquake triggered at least 1,218 landslides (Serey et al., 2019). This number is lower than the 3,477 landslides estimated for the Mw 9.0 Tohoku-Oki megathrust event (Wartman et al., 2013) and much lower than for shallow, smaller magnitude crustal earthquakes such as the 2008 Mw 7.9 Wenchuan earthquake (with close to 200,000 landslides; Fan et al., 2018) or the 1999 Mw 7.3 Chi Chi

earthquake (with >10,000 landslides; e.g., Khazai & Sitar, 2004). The landslides induced by the Maule earthquake were mostly disrupted landslides such as shallow slides and rock falls, according to Keefer's (1984) classification of coseismic landslides. In total, the volume of landslide material was on the order of 10^6 m^3 (Serey et al., 2019).

The Maule earthquake also disturbed the hydrological cycle, as observed from microcatchments (<4.5 km^2) located in the Coastal Cordillera (Mohr et al., 2012) and regional-scale catchments monitored by the Chilean *Dirección General de Aguas,* DGA (up to 2.08×10^4 km^2). Accumulated excess streamflow discharge amounted to at least 1.1 km^3, which is the largest volume reported after an earthquake (Mohr et al., 2017). The coseismic disturbances may have affected the circulation of fluids in very shallow unsaturated soils (Mohr et al., 2015), shallow saturated soils (Mohr et al., 2012), and in deep hydrothermal reservoirs (Pritchard et al., 2013). In recent years, attempts to test hypotheses explaining that response have generally favored changes in permeability (Mohr et al., 2017).

So far, no megaturbidite deposits attributable to the Maule earthquake have been detected in lakes, in contrast to the giant 1960 Valdivia earthquake (Mw 9.5; Van Daele et al., 2015). For the Maule earthquake, Van Daele et al. (2015) described mass transport deposits and two types of lacustrine turbidites (LT1 and LT2; Figure 1c). Mass transport deposit and LT1 originated from downslope movements of sediments initially deposited on the lacustrine slopes. In contrast, LT2 presents more terrestrial facies, fed from subaerial mass wasting events or delta collapses (Van Daele et al., 2015). The LT2 deposits have been identified in six lakes with local MM intensities > VI. However, localized subaerial mass wasting events occurred only in the two northernmost lakes, which likely represent the sources of these deposits (Figure 1c).

4. Materials and Methods

4.1. Suspended Sediment Records

Daily measurements of the suspended sediment concentration (*SSC*, in mg/l) and streamflow discharge (Q, in m^3/s) were carried out by the DGA (http://www.dga.cl/). See Solar (1999) and Text S1 in the supporting information for sampling descriptions. Details of our revision of stream gauge locations and procedures for delineation of catchments (Holmgren, 1994; Jenson & Domingue, 1988; Tarboton, 1997) are in Text S2.

From the 87 gauges, we selected data from 32 draining catchments affected by seismic intensities >V (latitudes 31–40°S), which contained at least 1 year of postseismic records. Thirty one of the 32 gauges containing more than 3 years of postseismic data were analyzed (Table 1). Sampling started in 1985 for most of the gauges (Carretier et al., 2018), providing decades of daily hydrometric values to constrain a preseismic baseline. Using this database, we estimated the average daily suspended sediment discharge (Q_s, in kg/s) as the product of the *SSC* and daily discharge Q.

4.2. Baseflow Separation

Previous work highlighted the decisive role that groundwater discharge may play for streamflow (Andermann, Crave, et al., 2012; Andermann, Longuevergne, et al., 2012) and the relevance of separating total streamflow (Q) into baseflow (Q_b, in m^3/s) and direct-flow (Q_d, in m^3/s) when interpreting sediment mobilization in mountainous areas (Andermann, Crave, et al., 2012; Andermann, Longuevergne, et al., 2012; Tolorza et al., 2014). Our key assumption is that sediment mobilization is restricted to the channel network for periods when Q_b=Q, whereas larger parts of the catchment (e.g., hillslopes) may be involved when Q_d>0 (e.g., Andermann, Crave, et al., 2012; Tolorza et al., 2014). Surface processes triggered by the Maule earthquake include disturbances that may modify the sediment transport under differing stages of streamflow. Coseismic and postseismic landslides may feed the river network when hydrologic connectivity is established between landslides and rivers, that is, during rainfall-runoff events. In contrast, the rapid release of water recorded after the earthquake occurred during low-flow conditions, thus potentially remobilizing the postseismic sediment within channels or floodplains. In addition, the dynamics of sediment transport in the postseismic period were characterized by low streamflow due to the severe drought. To compare such drought-restricted river flow with other periods of comparable hydrologic conditions, we isolated sediment fluxes that occurred during baseflow conditions from sediment exported when we assume a large fraction of the catchment contributed to rainfall-runoff (i.e., during storm flow conditions). To this end, we applied a recursive baseflow filter (Ladson et al., 2013; Natahan & McMahon, 1990), available in R's *hydrostats*

Table 1
Basic Data From the Hydrometric Stations From Which Postquake Measurements Are Available

Id	St. Name	River	St. Code	Drainage area [km^2]	N prequake data Period PRE-1	Period PRE-2	Period PRE-3	N postquake data Period POST-1	Period POST-2	E[mm/a]
1	Cuncumen	Choapa	04703002	1110	8003	1088	1325	2948	1068	0.01
2	Las_Burras	Illapel	04721001	600	13600	1053	1304	2207	1089	0.00
3	Chacabuquito	Aconcagua	05410002	2106	6314	1091	796	2514	890	0.09
4	Resg_Los_Patos	Putaendo	05414001	884	6367	720	940	2459	849	0.02
5	El_Manzano	Maipo	05710001	4842	11830	776	944	1923	449	0.24
6	Los_Almendros	Mapocho	05722002	637	11652	822	1157	1957	403	0.05
7	Rinc_de_Maipu	Mapocho	05737002	4003	12645	806	1161	1314	514	0.04
8	Puente_T_Cauq.	Cachapoal	06008005	2453	2037	643	0	2348	694	0.10
9	Bajo_los_Briones	Tinguiririca	06028001	1441	4756	886	694	2365	601	0.17
10	Los_Quenes	Claro	07103001	352	10884	1066	1349	2830	1080	0.09
11	DJ_Claro	Teno	07104002	1205	11269	1091	1340	2866	1051	0.13
12	Sauzal	Purapel	07343001	406	7115	983	980	2369	1033	0.02
13	Las_Brisas	Loncomilla	07359001	9906	7770	1084	1234	2854	1060	0.02
14	San_Fabian_2	Nuble	08106002	1648	3346	1094	434	2045	1093	0.04
15	Cam_a_Confluencia	Chillan	08117005	758	6187	1095	923	2834	1079	0.02
16	Cholguan	Itata	08123001	867	7271	997	1366	2818	1039	0.02
17	Longitudinal	Diguillin	08132001	1324	6702	1094	944	2508	1066	0.02
18	Balsa_Nueva_Aldea	Itata	08135002	4499	6910	1093	1213	2816	1096	0.01
19	Coelemu	Itata	08141001	10216	6618	1091	1150	2742	1077	0.03
20	Llanquen	Biobio	08307002	3360	2510	1092	0	2832	1097	0.02
21	Tijeral	Vergara	08358001	2405	8540	971	1221	2689	1053	0.01
22	Puente_Perales	Laja	08383001	3565	6339	1090	1231	2272	547	0.02
23	Desembocadura	Biobio	08394001	24221	7257	1012	1243	695	695	0.02
24	Lumaco	Lumaco	09102001	1028	8537	995	1350	2715	994	0.01
25	Cholchol	Cholchol	09116001	5051	7176	1095	931	2790	1089	0.01
26	RariRuca	Cautin	09123001	1251	9086	1085	1352	2782	1029	0.04
27	Cajon	Cautin	09129002	2789	8871	1088	1350	2883	1051	0.02
28	Quepe	Quepe	09135001	1664	8610	1073	1302	2468	975	0.01
29	Los_Laureles	Allipen	09404001	1650	7006	1027	953	2733	1072	0.06
30	A_Llafquenco	Trancura	09414001	1412	8725	1062	1343	2730	1035	0.02
31	Gorbea	Donguil	09434001	746	8541	1093	1317	2298	1069	0.01
32	Rucaco	Cruces	10134001	1802	8605	1095	1317	2768	974	0.01

Note. Erosion rates (E, in mm/a) from Carretier et al. (2018).

package (Bond, 2016), to the entire streamflow time series. We then calculated basal and direct suspended sediment discharge (Q_{so} and Q_{sd}, respectively, in kg/s) and concentrations (SSC_o and SSC_d, respectively, in mg/l) for both conditions separately (i.e., when Q_b=Q and Q_d>0).

4.3. Hydroclimatology and Time Series Analysis

Our data cover years with highly variable hydroclimatic conditions. Both extraordinarily wet and dry periods occurred prior to and after the earthquake (e.g., Garreaud et al., 2017; Montecinos & Aceituno, 2003; Viale & Garreaud, 2014). Those conditions might affect thresholds for sediment mobilization on hillslopes (for landsliding and for runoff generation) and in rivers (detachment threshold). Indeed, the geomorphic work of successive and moderately intense rainfall-runoff events differs from that triggered by high intensity-low frequency events, thus affecting not only the mean sediment fluxes but also their entire distribution (e.g., Andermann, Crave, et al., 2012; Andermann, Longuevergne, et al., 2012; Mohr et al., 2014; Tolorza et al., 2014). This might be particularly relevant given the drought conditions of the postseismic period. In order to account for such differences for the whole range of streamflow conditions (i.e., over the entire streamflow regime), we calculated (1) the peak, mean, and various percentiles (95th, 90th, 75th, 50th, and 25th) for Q, Q_s, SSC, Q_{so}, and Q_{sd} for different time-windows and (2) the postseismic/preseismic ratio of each quantile for the 31 stations with more than 3 years of postseismic data. To this end, we considered the following time windows:

1. The total preseismic data available (period PRE-1: 1985 to February 2010).
2. The latest 3 years of the preseismic period (period PRE-2: February 2007–2010).
3. The driest intervals of the preseismic period (period PRE-3: all the data recorded during the strong negative ENSO phases of April 1988 to May 1989 and July 1998 to February 2001).
4. The total postseismic period, up to 2018 (period POST-1: February 2010–2018).
5. The 3-year postseismic period (period POST-2: February 2010–2013).

The comparisons consist of ratios between quantiles of the (a) POST-1/PRE-1, (b) POST-2/PRE-2, and (c) POST-2/PRE-3 periods.

4.4. Sediment Rating Curves

We calculated the suspended sediment rating parameters (SSRs), which describe the relationships between SSC and Q in addition to SSC_d and Q_d, that is, the κ and κ_{direct} coefficients and the b and b_{direct} exponents of the fitted power laws:

$$\text{SSC} = \kappa Q_d^b \tag{1}$$

$$\text{SSC}_d = \kappa_{\text{direct}} Q_d^{b_{\text{direct}}} \tag{2}$$

where κ was reported to increase after the Chi-Chi earthquake using a fixed value of b in order to compare changes in κ for unit discharge (Dadson et al., 2004; Hovius et al., 2011). However, Huang and Montgomery (2013) observed systematic changes in both parameters—κ and b—following a change in the regional sediment transport regime after the Morakot typhoon in Taiwan. A decrease in b together with an increase in the intercept κ resulted in much greater sediment concentration during the subsequent low-flow events after the typhoon. Given the drought during the postseismic period, and thus a higher proportion of low-flow data with respect to the preseismic period, we did not fix but let b vary in order to explore the entire parameter space of the inverse power law model. SSRs were calculated based on (i) the entire PRE-1 period and (ii) the data for each hydrologic year. In order to determine the best fit values of κ and b, as well as their uncertainties, we performed a maximum likelihood estimation on parameters of the linear regression model of the log transformation of equations (1) and (2), assuming that the error terms of the regression model are normally distributed. In practice, the κ and b parameters are found by maximizing the maximum likelihood estimation function.

4.5. Other Environmental Parameters of Catchments

With the aim of quantitatively describing the catchments, we calculated the following basin-specific properties:

4.5.1. Hillslope Gradient

Steep slopes enhance landslides and the mobilization of sediments to rivers (e.g., Roback et al., 2018). To characterize the steepness of the studied catchments, we calculated the mean, median, and third quartile of hillslope gradient, as well as the percent area of hillslope gradient greater than 30° (see Figure S2 for the distribution of the hillslope gradients within the selected catchments). The critical hillslope gradient for landsliding depends on several site-specific conditions including the soil properties, vegetation, and water content. Most coseismic landslides of the Maule earthquake occurred within areas with a local slope of 20–40° according to the estimations of Serey et al. (2019) from the 30 m ASTER GDEM. Here we used a single cutoff value of 30° in order to highlight the slope distribution for a range of slope values for which hillslopes are more prone to failure. The hillslope gradient was obtained from (1) the 1 arc sec SRTM DEM based on a first-order derivative estimation and (2) a merged DEM based on a steepest descent estimation (Tarboton, 1997). The merged DEM includes data from TanDEM-X ©DLR 2017 12 and 30 m as well as SRTM 1 arc second, resampled to 12 m (see Figure S4 for the locations of tiles with different resolutions).

4.5.2. Vegetation

In the Mediterranean and temperate climate regimes, short-term erosion is highly sensitive to changes in the vegetation cover because exposed soils can be easily detached and mobilized by high-intensity rainfall during the humid seasons (Mohr et al., 2014; Schuller et al., 2013). Bare soils and rocks are prone to release sediments rapidly. Both shrubland and pastures may also promote sediment transport due to the low density and seasonal loss of vegetation. Bare soils, bare rock, and sparsely vegetated areas also may include

disturbances such as volcanic deposits and wildfires, with potentially high impacts on sediment fluxes (e.g., Major et al., 2016; Wagenbrenner & Robichaud, 2014). We used the Chilean Land Cover map provided by Zhao et al. (2016), which was obtained from LANDSAT 2014 images, and grouped the land surface into eight land cover classes, including bare soils, bare rock, shrublands, and pastures (see Table S1 in the supporting information for definitions of erodible covers and Figure S5 for maps). We also calculated the mean percent of tree cover based on Hansen et al. (2013).

4.5.3. Lithology

Two observations suggest a first-order control of lithology on the generation of coseismic landslides by megathrusts: (i) landslides triggered by the Maule earthquake in the Coastal Cordillera tend to cluster in soft lithologies, such as sandstones and limestones (Serey et al., 2019), and (ii) most of the landslides triggered by the Tohoku earthquake affected the youngest (Neogene) geologic units, while coseismic debris mobilization was controlled by lateral spreading within Quaternary sediments (Wartman et al., 2013). To characterize the hardness of rocks within catchments, we distinguish between two major lithologic groups based on the 1:1000000 geologic map (Sernageomin, 2003). Here *hard lithologies* include intrusive, hypabyssal, metamorphic, and older Mesozoic volcanic and sedimentary units. We define *soft lithologies* as geologic groups composed of Cenozoic sedimentary and volcano-sedimentary rocks (see Figure S3 for the distributions of hard and soft lithologies as well as Table S2 for the attributes that define the rock groups).

4.5.4. Earthquake

We calculate the following parameters to describe the impact of the ground motion within the catchment boundaries: (i) the maximum horizontal PGA from Boroschek et al., 2012) and the USGS (2010); (ii) the maximum seismic intensities, considering data from Astroza et al. (2012), Van Daele et al. (2015), and USGS (2010); (iii) the volumetric sum of landslides activated by the earthquake; (iv) the volumetric sum of landslides activated by the earthquake normalized by the catchment area; and (v) the sum of the landslide areas divided by landslide distance to streams. The coseismic inventory was built by Serey et al. (2019) including previous unpublished works (Escobar, 2013; Moya, Sepúlveda, Serey, García, et al., 2015; Moya, Sepúlveda, Serey, Montalva, et al., 2015; Serey et al., 2017). Methods for volume estimates (Larsen et al., 2010) are briefly described in the Text S3. The distance to streams represents the horizontal distance between the centroid of the landslide and streams calculated with the procedures described in Text S2. Specifically, this distance was computed using the GRASS GIS tool *v.distance*.

4.5.5. Sediment Traps

Lakes and reservoirs act as sediment traps within the river catchments, disconnecting and buffering the downstream propagation of catchment-wide erosive responses (e.g., Fryirs, 2013). We compiled georeferenced information of natural and artificial water bodies (Chilean Congress National Library, https://www.bcn.cl/siit/mapas_vectoriales/, 08/30/2018), which we complemented with updated information of hydro-electric reservoirs (Chilean Commission of Energy, http://datos.energiaabierta.cl/dataviews/228007/centrales-hidroelectricas/, 30 August 2018) in order to account for the recent number of lakes and reservoirs within the catchment areas. The influence of an individual sediment trap for downstream sediment transfer is likely to depend on its upstream contributing area. We estimate that area by identifying the maximum value of the *accumulation raster* within the lake or reservoir polygon. The *accumulation raster* is the output of *r.watershed* that accounts for the number of cells that drain through each cell. The estimated upstream contributing area was used to weight the relative importance of each sediment trap.

4.6. Random Forest

We used the Random Forest (RF) regression method (Breiman, 2001) to identify the catchment and earthquake-related controls that determine the changes in SSC and Q_s before and after the Maule earthquake. The RF consists of ensembles of decision trees trained on data, forming a robust nonparametric statistical model. The RFs are capable of handling nonlinear, noisy, fragmented, or even correlated multidimensional data. The RF may be used for both classification and regression (Liaw & Wiener, 2002; Strobl et al., 2008). Its core is the combination of bootstrap aggregation with random variable selection (Breiman, 2001). The RF explores the importance of predictors using bootstrapped data and predictor subsets for growing decision trees. In the RF, each tree node is split into two groups using the best among a subset of predictors that are randomly chosen at that node. The split follows a simple minimization of the total variance. An advantage of the RF is its robustness against overfitting (Breiman, 2001; Liaw & Wiener, 2002). At each bootstrap iteration, the RF predicts the data not included in the bootstrap data

(so-called "out-of-bag" data) using the tree grown on the bootstrap sample. After aggregating all of the out-of-bag predictions, RFs estimate the overall error rate by major vote (Breiman, 2001). The relative loss of model performance when omitting a specific predictor defines that predictor's importance, provided that it is corrected for spurious correlation effects (Strobl et al., 2008).

Our response variables are the ratios between preseismic and postseismic SSC and fluxes (see section 4.3 and Table S3). Predictor variables include the ratios of continuous data on streamflow discharge over the timing of the earthquake (see section 4.3), geology, land cover, topography, and earthquake properties (Table S4). We grew the RF with 1,000 individual trees. The number of variables at each node ranged between 12 and 19 (out of a total of 34 predictors). Although this setup is higher than the recommended number of nodes (Liaw & Wiener, 2002), the model performance was best when using that value. The number of predictor variables is largely considered as a tuning parameter (Hastie et al., 2009). We performed all calculations using R's *randomForest* package (Liaw & Wiener, 2002).

We iteratively performed RF models and selected the results with a positive correlation between the observed and predicted values considering a threshold $R^2 \geq 0.5$ (Data Sets S1 and S2 in the supporting information). To rank the contributions of different environmental controls as predictors of postseismic sediment concentrations and fluxes, we quantified their relative importance in terms of the total added predictive accuracy and node purity. The latter is a measure of the difference between the residual sum of squares before and after the split on that specific predictor.

5. Results

5.1. Postseismic suspended sediment exportation in the decennial context

For almost all of the analyzed hydrometric stations (n=30, 29, and 25 for the three comparisons; Figures 2a–2c, respectively), the mean values of Q_s during the postseismic period are equal to or lower than those of the preseismic periods. Exceptions of higher postseismic mean Q_s include station 3 (Figure 2a: all postseismic vs. pre seismic data), stations 3 and 5 (Figure 2b: 3 postseismic vs. 3pre seismic years), and stations 5, 14, 27, and 32 (Figure 2c: dry-period ratios). The reduced postseismic mean Q_s at most stations is consistent with the lower mean Q: ratios of mean streamflow discharge are lower than 1 for all the stations in Figures 2a and 2b and lower than 1 for 24 of the 29 stations that were compared in Figure 2c. This illustrates the severity of the drought affecting those time series, even when the postseismic data are compared with other dry periods. The mean *SSC*, however, is higher in the postseismic periods for several catchments (Figure 2). These catchments are characterized by steep slope gradients and low vegetation cover.

Five stations show distinctive peaks of *SSC* (Figure S6) at the beginning of the 2012 hydrologic year, 2 years after the Maule earthquake (stations 1, 3, 8, 9, and 11). Among them, the Chacabuquito station contains the most complete record (Figures 3a–3c). This station reached its historic *SSC* peak on 27 May 2012, during the first large rain storm after the Maule earthquake occurred. According to the CR2MET daily rainfall product (DGA, 2017), this storm yielded 58.6 mm on average across the catchment the day before (26 May 2012; Alvarez-Garreton et al., 2018).

We observe only six stations (stations 1, 3, 4, 5, 6, and 14) where postseismic SSRs clearly exceed the long-term power law trend. These catchments are all located in the Principal Cordillera and have the steepest slopes of all studied catchments, exhibiting a high percentage of bare soils (Figure 2). In contrast, the postseismic SSRs at eight stations (12, 13, 16, 21, 24, 25, 26, and 29) cluster below the long-term preseismic power law trend. Interestingly, these stations include the catchments that are located in the Coastal Cordillera nearest to the rupture area, which experienced the highest PGA (i.e., station 12: Purapel en Sauzal, station 21: Vergara en Tijeral, and station 24: Lumaco en Lumaco; Figures 3d–3f).

Most of the postseismic rating coefficients κ and b (at 29 out of 31 stations) lie within the long-term variability for individual hydrologic years. This is true both for the Q-SSC and the Q_d-SSC_d relationships. Nonetheless, 10 stations experienced higher κ and lower b values for the postseismic hydrologic years when compared to preseismic conditions (stations 3, 5, 11, 14, 18, 19, 26, 28, 29, 30, 31, and 32).

Figure 4 shows the ratios between quantiles of Q_s, Q_{sd}, and Q_{so} of the postseismic and preseismic periods. The Q_s ratios are concentrated below 1 in all cases (Figures 4a–4c), with the lowest concentration for POST-2 quantiles compared to those of the PRE-3 period (dry years of the preseismic background). The

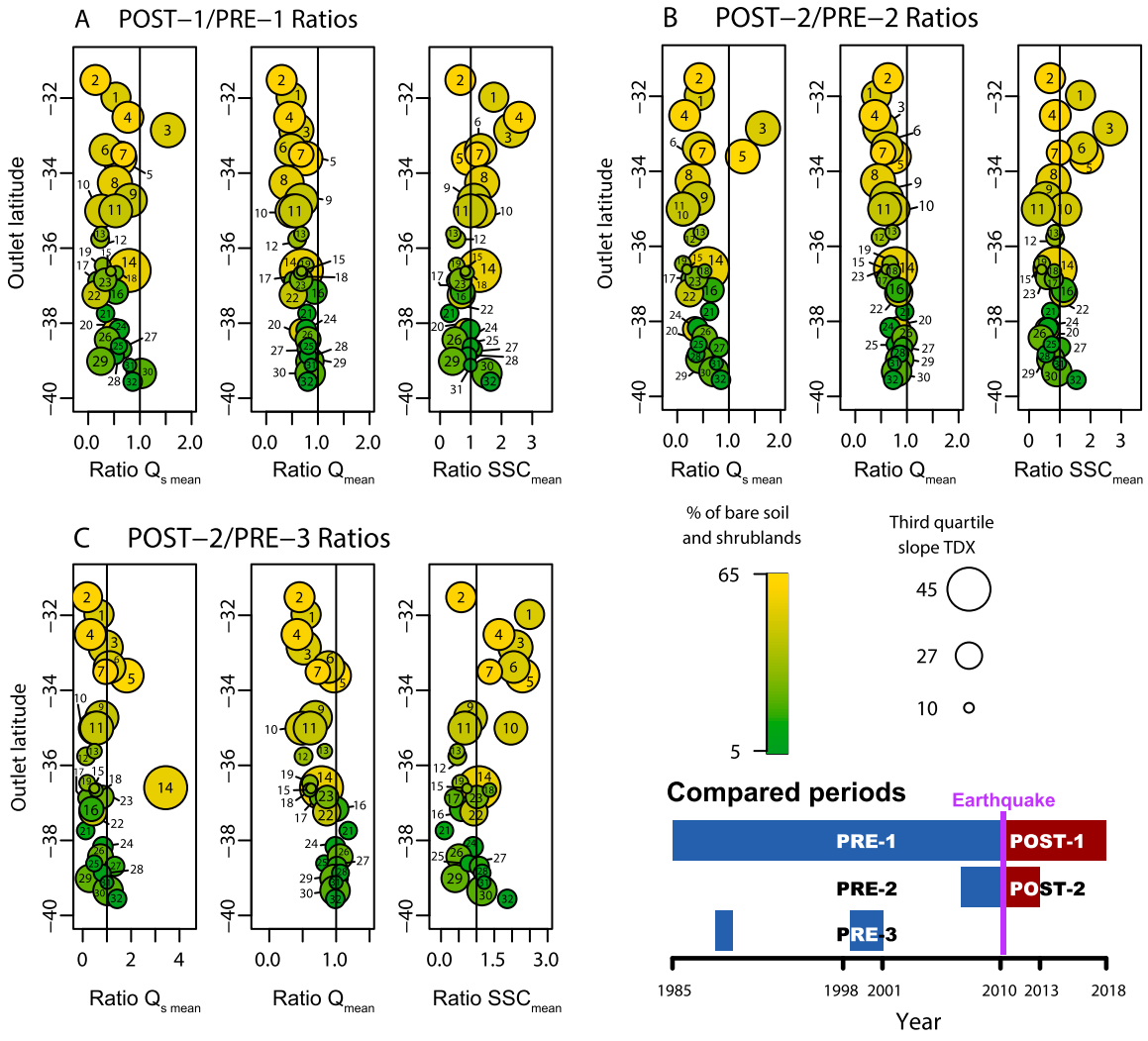

Figure 2. Postseismic/preseismic ratios between the mean values of hydrometric parameters for the following periods: (a) POST-1/PRE-1 (full postseismic period/full preseismic period), (b) POST-2/PRE-2 (3-year postseismic period/3-year preseismic period), and (c) POST-2/PRE-3 (3-year postseismic period/driest preseismic period). Circles are colored according to the percent of the catchment covered by bare soil and shrublands, according to Zhao et al. (2016), and are sized according to the third quartile of the topographic gradient, which was calculated with TanDEM-X ©DLR 2017 (12 and 30 m resized to 12 m; see Figure S4).

response of the Itata River is notable as the postseismic sediment yield was lower than that of the preseismic periods, despite the fact that it experienced approximately a fivefold postseismic increase in streamflow (Mohr et al., 2017).

The results are distinct if we treat the baseflow and storm flow separately. In spite of the similarity between the Q_s and Q_{sd} ratios (Figures 4a–4f), the base suspended sediment flow Q_{so} increased after the earthquake for a larger number of gauges (Figures 4g–4i), and these include several ratios that are 2 to 4 times the Q_s and Q_{sd} ratios. More than half of the stations recorded higher postseismic values for the 25th percentile of Q_{so} in the case of the three comparisons, while the entire distribution of Q_{so} ratios comprises values >1 for 14 to 24 stations (Figure 4i).

5.2. Environmental Controls on Suspended Sediment

We obtained 67 robust RF models ($R^2 \geq 0.5$) to predict *SSC* ratios and 117 to predict Q_s ratios. In both cases, we counted the times that each predictor was ranked among the five most important (Figure 5). By far, predictors describing bare to sparsely vegetated cover and hillslope gradient, which are illustrated in Figure 6, were the most important for predicting changes from preseismic to postseismic *SSC*. Moderate and high

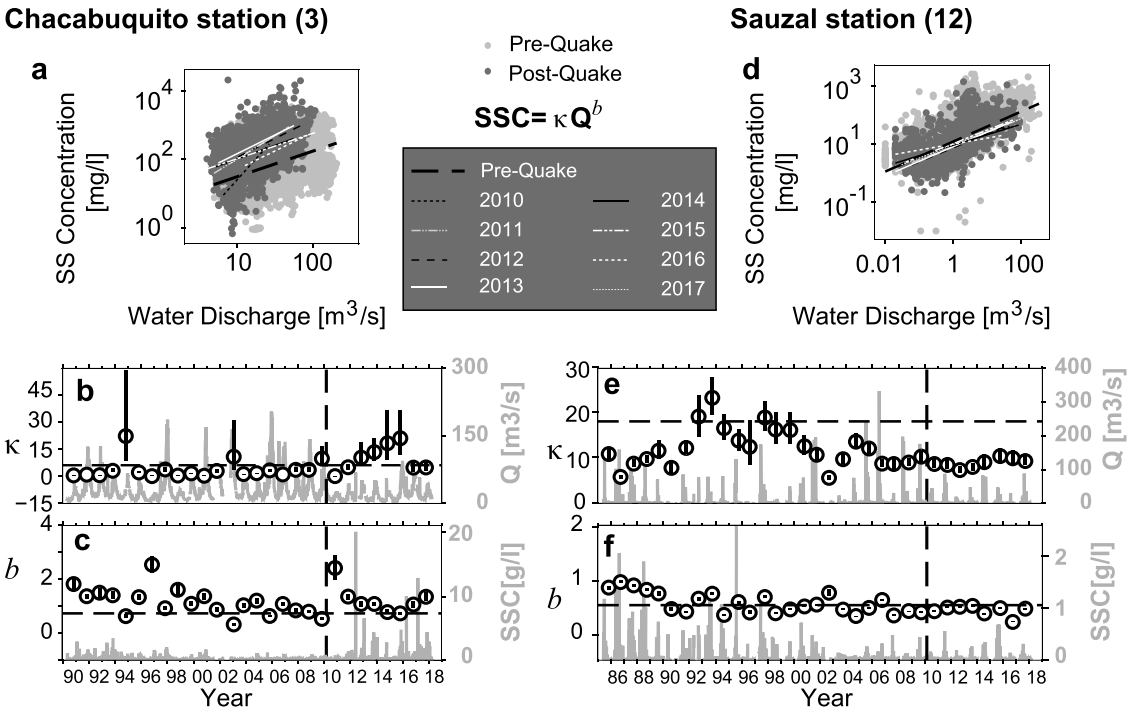

Figure 3. Hydrometric variability at the Chacabuquito and Sauzal stations (see drainage areas in Figure 1b). (a and d) Correlation diagrams between Q and SSC, as well as the power law fits using all prequake data and individual postseismic hydrologic years. (b and e) Time series for the daily Q (gray) and interannual variability of the κ coefficient. (c and f) Time series of the daily suspended sediment concentration (SSC; dark gray) and interannual variability of the b coefficient. Data for 2018 were not available for the entire hydrologic year and therefore are excluded. The dashed horizontal line represents the κ and b coefficients of all preseismic data. Both coefficients are obtained from optimization of a maximum likelihood estimation of the log transformation of equations (1) and (2), assuming a normal distribution of errors. The dashed vertical lines indicate the date of the earthquake.

water discharge ratios in the comparison between dry-years (POST-1/PRE-3 ratios) and sediment traps also showed some impact by their contribution to node purity and overall accuracy of RF models, respectively. In contrast, none of the predictors describing the erosional resistivity of the lithology, the seismic intensities, PGA, and coseismic landslides within catchments exhibited significant impact. Results improved by including hillslope gradient and bare to sparse vegetation cover. Yet for the specific comparison of the postseismic Q_s with respect to other dry years, the best predictors were the Q_{median} and Q_{peak} ratios.

Taken together, our RF modeling exercise identified the combination of bare soil and hillslope gradient as the best combination to predict environmental controls for changes in both SSC and Q_s (Figure 5). When focusing on dry conditions, however, moderate to high water discharge also emerged as relevant predictors.

6. Discussion

6.1. Sediment Fluxes After the Maule Earthquake

Most of the 31 monitored streams showed a reduction in suspended sediment flux in the 3–8 years following the earthquake for moderate to high values of the Q_s and Q_{sd} distributions (mean, median, 75–95th percentiles, and peaks) compared to background values. Only the lower fraction of sediment fluxes (those under 25th percentile of Q_s) and the base sediment fluxes (sediment fluxes under base streamflow conditions, Q_{so}) were higher than the preseismic background for most gauges. This is particularly true in comparison with other dry periods.

Our knowledge of landslides activated by this specific earthquake is restricted to the co-seismic period (Serey et al., 2019). However, studies of other regions and climates indicate that post seismic increase in landslide rates (Marc et al., 2015) and catchment-wide erosion (Hovius et al., 2011; Wang et al., 2015) may last several years. From 27 February 2010 to present, most of the studied Chilean rivers have not yet shown an increase in their moderate to high sediment fluxes (Figures 3 and 4). We can therefore consider this seismic event as

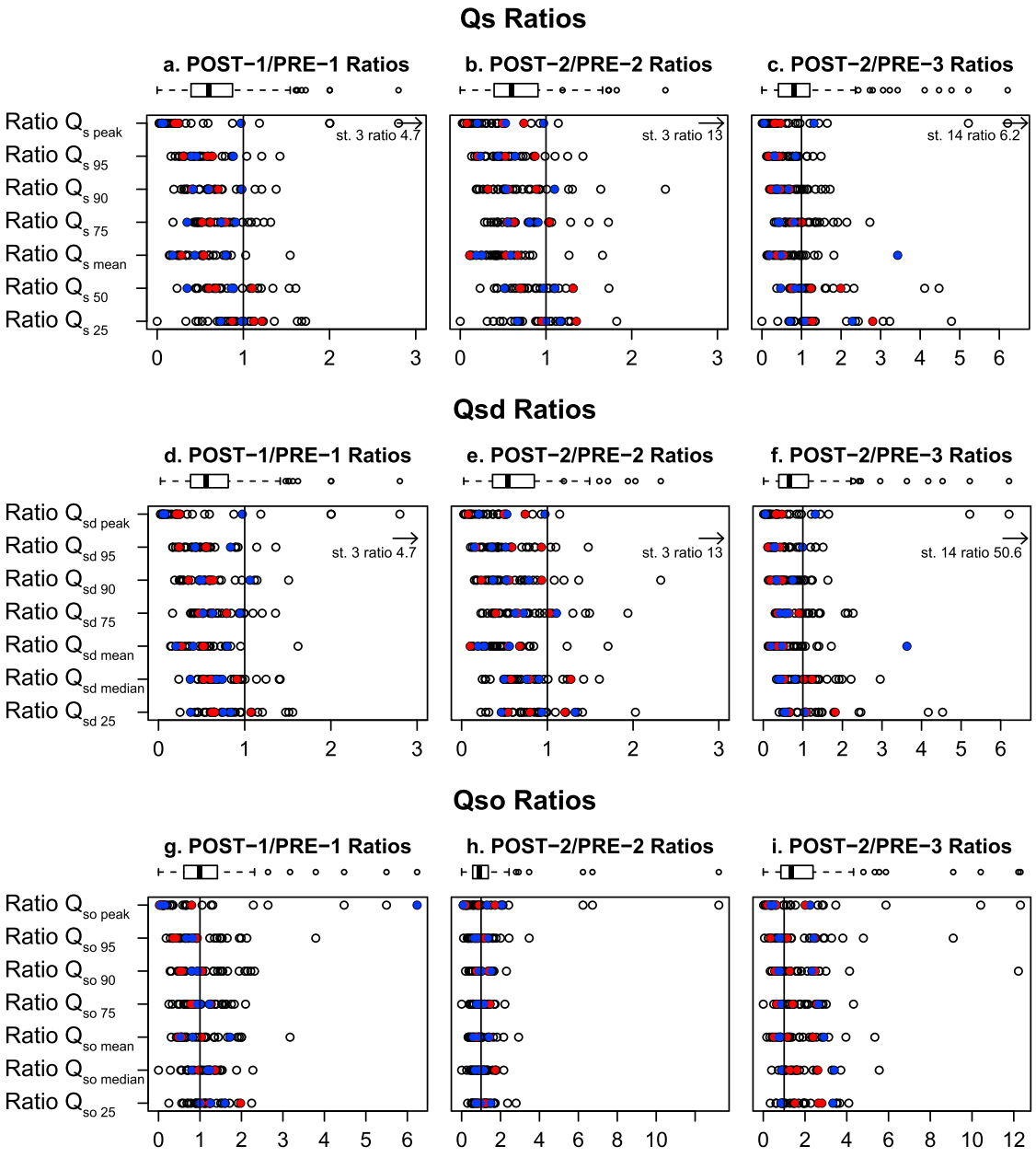

Figure 4. Postseismic/preseismic ratios of quantiles of the suspended sediment discharge (Q_s), and the direct (Q_{sd}) and base (Q_{so}) suspended sediment discharge for the three evaluated preseismic periods. The red and blue points are records from the Itata River and its tributaries, respectively. Arrows in a–f indicate the position of a single outlier (labeled below the arrow).

not particularly erosive, despite its high magnitude. This finding is counterintuitive at first glance. However, our results are consistent with both Marc et al. (2016), who analyzed a database of 40 earthquakes, and with the small number of large landslides attributable to megathrust earthquakes in the Chilean Andes (Antinao & Gosse, 2009). In addition, Mohr et al. (2014) did not find an impact of the Maule earthquake on sediment transport in small headwater catchments of the Coastal Range. Here we demonstrate the limited impact on catchment-wide erosion for one of the largest surveyed subduction earthquakes along a region that is characterized by variable precipitation rates, slopes, and vegetation cover. Our study therefore confirms the need to evaluate other parameters when predicting landslide and erosion responses to earthquakes, aside from the magnitude alone.

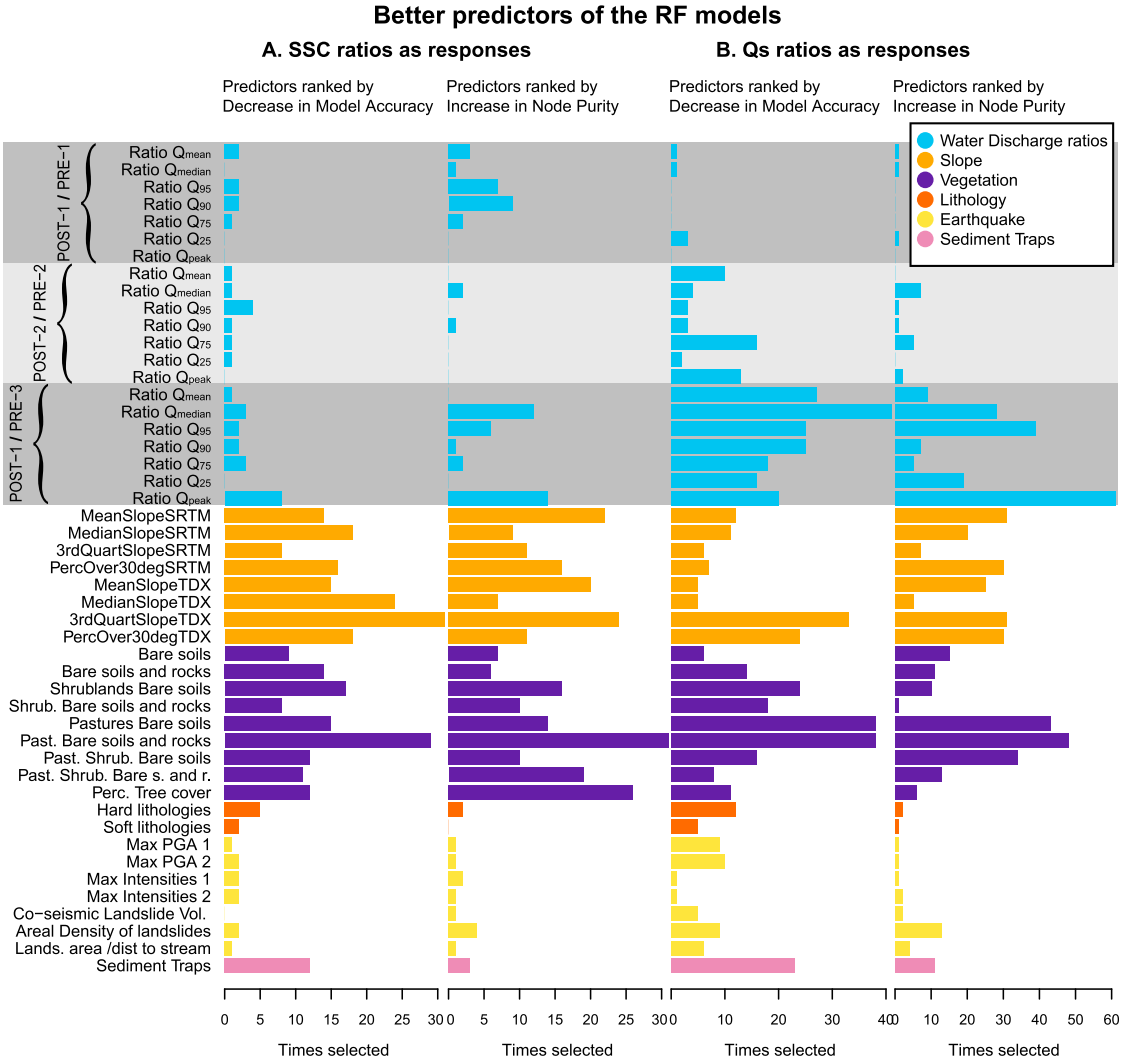

Figure 5. Histogram of ranked predictors conditioned by response classes of Random Forest (RF) models ($R^2 \geq 0.5$) in terms of increased accuracy and increased node purity. (a) Results of 67 RF models predicting ratios of suspended sediment concentrations (Data Set S1). (b) Results of 117 RF models predicting ratios of suspended sediment fluxes (Data Set S2). See Table S4 for details of predictors.

6.2. Controls on Postseismic Suspended Sediment

The Maule earthquake triggered sediment pulses in lakes up to a distance of 200–260 km from the main rupture area (slip >1–10 m; Figures 1a and 1c) due to local seismic intensities that exceeded MMI VI (Figure 1b; Van Daele et al., 2015). However, most of these deposits were fed from lake slopes and delta collapses. Hence, we argue that this constitutes remobilization and resedimentation rather than the occurrence of primary erosion and that the sediment sources were restricted to subaqueous environments. These subaqueous slides were likely triggered by increased pore water pressures due to cyclic seismic loading (Wang & Manga, 2011). In terrestrial environments, the Maule earthquake triggered at least 1,218 co-seismic landslides of small to moderate size (i.e., 10.6×10^6 m^3; Serey et al., 2019). Given the relatively small number of co-seismic landslides compared to other large earthquakes (section 3) and the severe drought during postseismic conditions, the Maule earthquake did not produce an immediate sediment pulse for the 32 monitored river gauges (Figure S6). Of the coseismic landslides, approximately half occurred within gauged catchment (Figure 1c). The relatively low number of triggered landslides is consistent with the high erosional resistance of the granitic and metamorphic lithologies of the Coastal Cordillera. In fact, mass wasting events in the Coastal Range were concentrated in areas with relatively low resistance sedimentary rocks of the Arauco

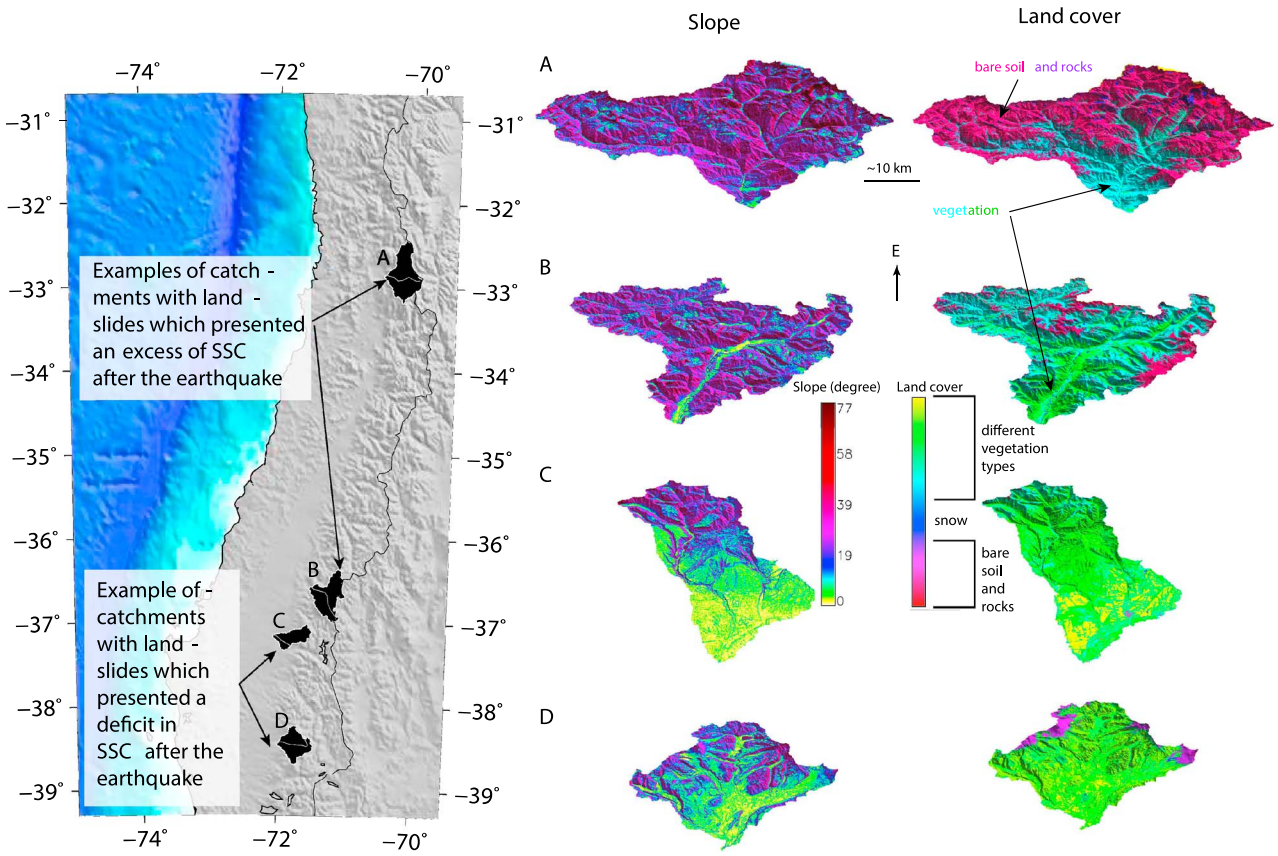

Figure 6. Illustration of catchments presenting an excess/deficit response and the best predictors selected by the Random Forest (RF) models.

Peninsula (Moya, Sepúlveda, Serey, García, et al., 2015; Moya, Sepúlveda, Serey, Montalva, et al., 2015). However, this observation is not repeated in the Principal Cordillera (Serey et al., 2019). Our RF-model does not support a lithologic impact on the postseismic *SSC* and Q_s (Figure 5). We are therefore inclined to conclude that the general lithologic contribution for controlling catchment-wide postseismic erosion is minor, at least for the monitored catchments and excluding the Arauco Peninsula. Another control on the relatively low coseismic landslide population may be the recurrence of seismic disturbances, reducing the supply of hillslope material susceptible to failure during subsequent events. Assuming a legacy effect of former earthquakes, a latitudinal gradient in coseismic landsliding mimicking the spatial patterns of seismic intensity and PGA of the giant Valdivia earthquake is plausible, at least in the Principal Cordillera where lithologies are similar from north to south. However, such a pattern is not supported by the coseismic catalog of the Maule earthquake (Figures 1c and S1; Serey et al., 2019). Hence, we can only speculate about the single effects of the Maule and Valdivia earthquakes on overall hillslope stability and sediment supply. Disentangling the individual effects of subsequent disturbances remains challenging given the data scarcity prior to and after individual disturbances (Mirus et al., 2017).

The erodibility of the soil surface and topographic slope exerted strong controls on suspended sediment before and after this earthquake. Our RF models clearly identify bare to sparsely vegetated areas and the hillslope gradient as the most important predictors for the observed *SSC* and Q_s ratios (Figure 5). This is even more the case, when comparing postseismic suspended sediments with dry years prior to the earthquake, when the system becomes more sensitive to changes in medium and high water fluxes. These results reflect a landscape that is prone to diffusive erosion, which is consistent with densely stocked forest plantations along the hillslopes in Central Chile (Miranda et al., 2017). Observations at the hillslope scale (Banfield et al., 2018; Soto et al., 2019) and models at the catchment scale (Rodríguez-Echeverry et al., 2018) indicate that Chile's intense forestry practices promote soil erosion by enhancing surface runoff. Furthermore, previous studies provide evidence for a runoff mechanism that is mainly controlled by saturation excess

overland flow in areas mostly affected by the earthquake, even under drought conditions with rainfall-runoff events restricted to the rainy winter seasons (e.g., Mohr et al., 2013, 2014). Assuming a dominance of erosive saturation excess overland flow for the mobilization of hillslope sediment, high rainfall intensities are not required to promote erosive overland flow. Instead, the antecedent, prolonged and moderately intense rainfall events are sufficient to drive erosive overland flow. This mechanism is in line with the recorded rainfall intensities along the studied basins, which captured moderate rainfall events after the earthquake (Alvarez-Garreton et al., 2018).

The Maule earthquake occurred at the end of the dry season and after a relatively dry hydrological year (Figure S7). Hence, it is plausible to assume dry or low soil water contents around the timing of the earthquake. Soils with low water content tend to be less susceptible to slope failures, simply due to their lower weight (e.g., Vorpahl et al., 2013) and higher shear strength when compared to saturated soils (Sidle & Ochiai, 2006). In addition, exotic tree plantations such as *Pinus radiata* and *Eucalyptus globulus*, which cover a considerable part of the most affected area, consume a majority of the rainwater (e.g., Huber et al., 2010). Hence, it is likely that the first postseismic rainfalls fed the vegetation rather than recharging soils or even percolating into deeper portions of the aquifer system.

Trees are also known to stabilize slopes by adding root enforcement to the total cohesion (e.g., Cohen & Schwarz, 2017). In addition, Mohr et al. (2015) provided theoretical evidence of earthquake-enhanced vegetation activity by supplying additional water for trees by seismically shaking water out of soils. Assuming a short-term positive effect on plants, enhanced root cohesion immediately after the earthquake could reduce the susceptibility of slope failure. Such a positive earthquake-vegetation feedback is consistent with the impact of the tree cover as a predictor in our RF models. Nevertheless, we can only hypothesize that this positive feedback exists as soil moisture and root strength data are sparse in the study region (Ghislaine et al., 2012; Mohr et al., 2012).

6.3. Responses of Postseismic Suspended Sediment and the Role of Connectivity

Although a majority of the observed sediment fluxes in the postseismic period is lower than the background fluxes for all comparisons, some stations in catchments draining the Principal Cordillera recorded historic peaks in *SSC* and Q_s and/or showed a rise in the sediment rating curves (Figure 1c). These positive responses, however, occurred after a delay of 2 years following the earthquake. They also remain decoupled from the location of coseismic landslides: catchments without a response, despite the occurrence coseismic landslides, and catchments showing a response without coseismic landslides are inconsistent with sediment fluxes driven exclusively by coseismic landsliding.

A wide range of processes could explain our observations. For example, the recent rise of the snowline (Garreaud et al., 2017), exposing an increasingly larger area to potentially erosive rainfall, which in turn may intensify the downstream transfer of sediment from glacial headwaters. This mechanism is plausible for explaining the delayed rise of peak *SSC* in catchments with or without coseismic landslides (that is, at stations 3, 8, 9, and 11 and station 1, respectively). Here however, we favor two other mechanisms. First, a hypothetical increase in the postseismic rate of landsliding, namely, that coseismic shaking in dry regolith or surface fractures increase the propensity for subsequent slope failure. This mechanism potentially results in a delayed landslide response. Second, a delay (at stations 3, 8, 9, and 11) or complete blockage (at stations 12, 13, 16, 21, 24, 25, and 26) of sediment fluxes due to restricted connectivity between coseismic and postseismic landslide deposits and the channel network during rainfall-runoff events.

We can only speculate about postseismic landslides, however, nearly 600 coseismic landslides supplied a potentially large volume (on the order of 4.6×10^6 m^3) of new sediment to the monitored catchments for subsequent routing. We may therefore expect enhanced sediment mobilization, at least in the majority of the catchments affected by landslides, mainly during large runoff events. Nonetheless, higher postseismic *SSC* was observed only in a few catchments and, following our RF results, ratios between postseismic *SSC* and Q_s relative to background rates are explained by (1) slope and vegetation (Figure 6), (2) changes in high and medium streamflow in drought conditions, and (3) the effect of sediment traps (Figure 5). Thus, following the concept of hydrological response units (Flügel, 1995), we argue that connectivity was restricted during the drought following the Maule earthquake. Furthermore, because connectivity (or lack thereof) dominates the postseismic response, we reject our hypothesis of erosive response being mostly controlled by coseismic landslides.

Hillslope gradients account for the potential energy that is needed for coseismic and postseismic landslides (e.g., Marc et al., 2015; Roback et al., 2018), and more generally for all surface processes involving sediment detachment and mobilization (Anderson & Anderson, 2010). Thresholds of rainfall intensity for the entrainment of any particle of a given size, including sediment from landslides, soil erosion, volcanic deposits, and anthropogenic contaminants, are related to certain flow velocities (Hjulström, 1939), which in turn are a function of slope gradient according to Manning's equation. Indeed, recent spatially explicit connectivity models of sediment transport from hillslopes to rivers are largely a function of the hillslope gradient, topographic ruggedness (Cavalli et al., 2013), and vegetation cover (Foerster et al., 2014). Consequently, from the results of our RF models, two of the most important predictors (hillslope gradient and vegetation cover) may describe variables that theoretically control sediment connectivity within the catchments (Borselli et al., 2008; Cavalli et al., 2013).

Connectivity, which we infer from hillslope gradient and vegetation cover, may thus explain the historic maximum *SSC* peaks and upward shift of SSR observed at the stations with the most favorable conditions for both the detachment and mobilization of sediment on hillslopes (i.e., the highest slopes with the lowest vegetation cover, Figures 2 and 3c). In these specific settings, the first postseismic intense rain storms in 2012 (Figure 3c) may have been sufficient to connect the coseismically mobilized sediments from the hillslopes to the channel network. Comparable responses occurred under more humid climatic conditions after the Wechuan and Chi-Chi earthquakes (Dadson et al., 2004; Hovius et al., 2011; Wang et al., 2015). Nevertheless, both these earthquakes had relatively shallow foci compared to the Maule earthquake and triggered 10,000–200,000 landslides, exceeding the number of landslides in this study by 1 to 2 orders of magnitude. Thus, we emphasize that the transferability of our study is limited when compared to other hydroclimatological conditions and seismic settings.

6.4. Response of Sediment Mobilization Under Low-Flow Conditions

Here we report a general decrease in the moderate to high sediment fluxes after the Maule earthquake. In addition, we found evidence of enhanced sediment transport during low flow conditions. We observed a postseismic shift in the parameters of the sediment rating curves toward lower b and higher κ values for 12 stations. This shift suggests higher postseismic sediment concentrations during low flows than the baseline obtained from all preseismic measures. This pattern is consistent with findings after the Morakot typhoon in Taiwan (Huang & Montgomery, 2013). Yet there is substantial scatter in the daily *SSC* for a given Q. Regardless, higher postseismic quantiles of Q_{so} (Figures 4g–4i) and higher postseismic 25th percentiles of Q_s (Figures 4a–4c) for roughly half of the stations support our interpretation. Hence, our results suggest a higher postseismic transport efficacy during baseflow conditions. The changes in low sediment fluxes may be attributable to the rapid coseismic release of water by rivers. The Maule earthquake affected the regional hydrology, mostly resulting in enhanced baseflows after the earthquake (Mohr et al., 2017). Coseismic landslide deposits that reached the river floodplains might then have been captured by postseismic 'flood waves', eventually resulting in enhanced transport-limited sediment fluxes during the postseismic drought.

7. Conclusions

Our study demonstrates that the Maule megathrust earthquake had a limited impact on the overall concentration and transport of suspended sediment loads in the Chilean Andes. We attribute this rather counterintuitive response to the drought that affected the region during and after the earthquake. Given the severity of the drought, postseismic increases in sediment flux were only observed during low-flow conditions. Under drought conditions, topography and vegetation cover best explain the sediment transport responses of the studied catchments. As such, our results reflect end-member climatic conditions, which may differ from responses in wetter environments. The results presented in this work contribute to the idea that seismically induced denudation and the evacuation of detached sediments are not necessarily a function of earthquake magnitude. Instead, hydroclimatic conditions, vegetation cover, soil erodibility, and topography may play first-order roles in the postseismic erosion response. For high-magnitude earthquakes, coseismic landsliding may be surprisingly low under dry climatic conditions, and more abundant for shallow intraplate earthquakes when compared to megathrust interplate earthquakes. Although sediment delivered by landslides may increase the sedimentation rates in sinks during interseismic periods, we argue that prolonged dry postseismic conditions increase the sediment residence

time within basins during transport to sinks. Consequently, our study has implications for benchmarking erosion rates after earthquakes preserved in the stratigraphic record.

Acknowledgments
This work was supported by the Chilean Comisión Nacional de Ciencia y Tecnología (CONICYT) and the Institut de Recherche pour le Développement (IRD). It is a contribution to the FONDECYT project 3160843, the LMI COPEDIM, Newton Fund NE/N000315/1 project, and the TanDEM-X DEM_GEOL0845, DEM_GEOL1209, and DEM_GEOL0707 projects. Geospatial and statistical analysis was performed using Grass GIS (GRASS Development Team, 2017), R (R Core Team, 2018) and GMT (Wessel et al., 2013). The indexed hydrometric database available in Data Sets S2 and S3 was measured and compiled with support from the Chilean Government. The authors are very grateful to José Miñano and María Soledad Orellana (*Dirección General de Aguas*) for allowing access to the government data. Public access to the not-indexed database is available at http://snia.dga.cl/BNAConsultas/reportes. We thank Brandon Schneider as well as three anonymous reviewers and the Editors John Buffington and Michele Bolla Pittaluga for their constructive comments, suggestions, and improvements.

References

Aceituno, P. (1988). On the functioning of the southern oscillation in the South American sector. Part I: surface climate. *Monthly Weather Review*, *116*(3), 505–524. https://doi.org/10.1175/1520-0493(1988)116<0505:OTFOTS>2.0.CO;2

Álvarez-Garretón, C., Mendoza, P. A., Boisier, J. P., Addor, N., Galleguillos, M., Zambrano-Bigiarini, M., et al. (2018). The CAMELS-CL dataset: Catchment attributes and meteorology for large sample studies – Chile dataset. *Hydrology and Earth System Sciences Discussions*, 1–40. https://doi.org/10.5194/hess-2018-23

Andermann, C., Crave, A., Gloaguen, R., Davy, P., & Bonnet, S. (2012). Connecting source and transport: Suspended sediments in the Nepal Himalayas. *Earth and Planetary Science Letters*, *351-352*, 158–170. https://doi.org/10.1016/j.epsl.2012.06.059

Andermann, C., Longuevergne, L., Bonnet, S., Crave, A., Davy, P., & Gloaguen, R. (2012). Impact of transient groundwater storage on the discharge of Himalayan rivers. *Nature Geoscience*, *5*(2), 127–132. https://doi.org/10.1038/ngeo1356

Anderson, R. S., & Anderson, S. P. (2010). *Geomorphology*. Cambridge: Cambridge University Press. https://doi.org/10.1017/CBO9780511794827

Antinao, J. L., & Gosse, J. (2009). Large rockslides in the Southern Central Andes of Chile (32-34.5degS): Tectonic control and significance for Quaternary landscape evolution. *Geomorphology*, *104*(3–4), 117–133. https://doi.org/10.1016/j.geomorph.2008.08.008

Araya, C., Cisternas, M., & González, F. (2014). Evolución morfológica del principal deslizamiento del Riñihuazo, generado por el terremoto de 1960. In *VIII Simposio Latinoamericano de Geografía Física - IV Simposio Iberoamericano de Geografía Física* (pp. 1018-1026). Santiago, Chile. https://doi.org/10.13140/rg.2.1.4403.9520

Astroza, M., Ruiz, S., & Astroza, R. (2012). Damage assessment and seismic intensity analysis of the 2010 (Mw 8.8) Maule earthquake. *Earthquake Spectra*, *28*(S1), S145–S164. https://doi.org/10.1193/1.4000027

Banfield, C. C., Braun, A. C., Barra, R., Castillo, A., & Vogt, J. (2018). Erosion proxies in an exotic tree plantation question the appropriate land use in Central Chile. *Catena*, *161*, 77–84. https://doi.org/10.1016/j.catena.2017.10.017

Bond, N. (2016). Hydrostats: Hydrologic indices for daily time series data. Retrieved from https://cran.r-project.org/package=hydrostats

Boroschek, R. L., Contreras, V., Kwak, D. Y., & Stewart, J. P. (2012). Strong ground motion attributes of the 2010 Mw 8.8 Maule, Chile, earthquake. *Earthquake Spectra*, *28*(SUPPL.1), S19–S38. https://doi.org/10.1193/1.4000045

Borselli, L., Cassi, P., & Torri, D. (2008). Prolegomena to sediment and flow connectivity in the landscape: A GIS and field numerical assessment. *Catena*, *75*(3), 268–277. https://doi.org/10.1016/j.catena.2008.07.006

Breiman, L. (2001). Random Forests. *Machine Learning*, *45*(1), 5–32. https://doi.org/10.1023/A:1010933404324

Campos, J., Hatzfeld, D., Madariaga, R., Lopez, G., Kausel, E., Zollo, A., et al. (2002). A seismological study of the 1835 seismic gap in south-central Chile. *Physics of the Earth and Planetary Interiors*, *132*(1–3), 177–195. https://doi.org/10.1016/S0031-9201(02)00051-1

Carretier, S., Regard, V., Vassallo, R., Aguilar, G., Martinod, J., Riquelme, R., et al. (2013). Slope and climate variability control of erosion in the Andes of central Chile. *Geology*, *41*(2), 195–198. https://doi.org/10.1130/G33735.1

Carretier, S., Tolorza, V., Regard, V., Aguilar, G., Bermúdez, M. A., Martinod, J., et al. (2018). Review of erosion dynamics along the major N-S climatic gradient in Chile and perspectives. *Geomorphology*, *300*, 45–68. https://doi.org/10.1016/j.geomorph.2017.10.016

Cavalli, M., Trevisani, S., Comiti, F., & Marchi, L. (2013). Geomorphometric assessment of spatial sediment connectivity in small Alpine catchments. *Geomorphology*, *188*, 31–41. https://doi.org/10.1016/j.geomorph.2012.05.007

Charrier, R., Pinto, L., & Rodríguez, M. P. (2007). Tectonostratigraphic evolution of the Andean Orogen in Chile. In *The Geology of Chilee* (pp. 21–114). London: Geological Society Special Publication. https://doi.org/10.1144/GOCH.3

Cohen, D., & Schwarz, M. (2017). Tree-root control of shallow landslides. *Earth Surface Dynamics*, *5*(3), 451–477. https://doi.org/10.5194/esurf-5-451-2017

Dadson, S. J., Hovius, N., Chen, H., Dade, W. B., Lin, J. C., Hsu, M. L., et al. (2004). Earthquake-triggered increase in sediment delivery from an active mountain belt. *Geology*, *32*(8), 733–736. https://doi.org/10.1130/G20639.1

Davis, S. N., & Karzulovíc, K. J. (1963). Landslides at Lago Riñihue, Chile. *Bulletin of the Seismological Society of America*, *53*(6), 1403–1414. Retrieved from https://dx.doi.org/

DGA. (2017). Actualización del balance hídrico nacional, SIT N°417 Ministerio de Obras Públicas. Santiago, Chile.

Escobar, P. (2013). Inventario de remociones en masa desencadenadas por el sismo del 27 de febrero de 2010 en Chile Central. Departamento de Geología, Universidad de Chile. Retrieved from http://tesis.uchile.cl/handle/2250/115454

Fan, X., Juang, C. H., Wasowski, J., Huang, R., Xu, Q., Scaringi, G., et al. (2018). What we have learned from the 2008 Wenchuan earthquake and its aftermath: A decade of research and challenges. *Engineering Geology*, *241*, 25–32. https://doi.org/10.1016/j.enggeo.2018.05.004

Farías, M., Charrier, R., Carretier, S., Martinod, J., Fock, A., Campbell, D., et al. (2008). Late Miocene high and rapid surface uplift and its erosional response in the Andes of central Chile (33°-35°S). *Tectonics*, *27*, TC1005. https://doi.org/10.1029/2006TC002046

Farías, M., Comte, D., Roecker, S., Carrizo, D., & Pardo, M. (2011). Crustal extensional faulting triggered by the 2010 Chilean earthquake: The Pichilemu seismic sequence. *Tectonics*, *30*, TC6010. https://doi.org/10.1029/2011TC002888

Farías, M., Vargas, G., Tassara, A., Carretier, S., Baize, S., Melnick, D., & Bataille, K. (2010). Land-level changes produced by the Mw 8.8 2010 Chilean earthquake. *Science*, *329*(5994), 916. https://doi.org/10.1126/science.1192094

Flügel, W.-A. (1995). Delineating hydrological response units by geographical information system analyses for regional hydrological modelling using PRMS/MMS in the drainage basin of the River Bröl, Germany. *Hydrological Processes*, *9*(3–4), 423–436. https://doi.org/10.1002/hyp.3360090313

Foerster, S., Wilczok, C., Brosinsky, A., & Segl, K. (2014). Assessment of sediment connectivity from vegetation cover and topography using remotely sensed data in a dryland catchment in the Spanish Pyrenees. *Journal of Soils and Sediments*, *14*(12), 1982–2000. https://doi.org/10.1007/s11368-014-0992-3

Fryirs, K. (2013). (Dis)Connectivity in catchment sediment cascades: A fresh look at the sediment delivery problem. *Earth Surface Processes and Landforms*, *38*(1), 30–46. https://doi.org/10.1002/esp.3242

Garreaud, R., Alvarez-Garreton, C., Barichivich, J., Boisier, J. P., Christie, D., Galleguillos, M., et al. (2017). The 2010-2015 mega drought in Central Chile: Impacts on regional hydroclimate and vegetation. *Hydrology and Earth System Sciences Discussions*, *21*, 6307–6327. https://doi.org/10.5194/hess-2017-191

Ghislaine, R., Güntner, A., Creutzfeldt, B., Wziontek, H., Klügel, T., Tume, P., et al. (2012). Relación de la variación del almacenamiento de agua local y el gravímetro superconductor en el Observatorio Geodésico TIGO, Concepción, Chile. *Obras y Proyectos*, *12*(12), 71–78. https://doi.org/10.4067/S0718-28132012000200006

Gorum, T., Korup, O., van Westen, C. J., van der Meijde, M., Xu, C., & van der Meer, F. D. (2014). Why so few? Landslides triggered by the 2002 Denali earthquake, Alaska. *Quaternary Science Reviews*, *95*(0), 80–94. https://doi.org/10.1016/j.quascirev.2014.04.032

GRASS Development Team. (2017). Geographic resources analysis support system (GRASS GIS) software, version 7.2. Retrieved from http://grass.osgeo.org

Hansen, M. C., Potapov, P. V., Moore, R., Hancher, M., Turubanova, S. A., Tyukavina, A., et al. (2013). High-resolution global maps of 21st-century forest cover change. *Science*, *342*(6160), 850–853. https://doi.org/10.1126/science.1244693

Hastie, T., Tibshirani, R., & Friedman, J. (2009). *The elements of statistical learning: Data mining, inference, and prediction* (Vol. 173). New York: Springer.

Hjulström, F. (1939). Transportation of detritus by moving water: Part 1. Transportation. In P. D. Trask (Ed.), *SP 10: Recent Marine Sediments* (pp. 5–31). Tulsa, Oklahoma: American Association of Petroleum Geologists.

Holmgren, P. (1994). Multiple flow direction algorithms for runoff modelling in grid based elevation models: An empirical evaluation. *Hydrological Processes*, *8*(4), 327–334. https://doi.org/10.1002/hyp.3360080405

Hovius, N., Meunier, P., Lin, C.-W., Chen, H., Chen, Y.-G., Dadson, S., et al. (2011). Prolonged seismically induced erosion and the mass balance of a large earthquake. *Earth and Planetary Science Letters*, *304*(3–4), 347–355. https://doi.org/10.1016/j.epsl.2011.02.005

Howarth, J. D., Fitzsimons, S. J., Norris, R. J., & Jacobsen, G. E. (2012). Lake sediments record cycles of sediment flux driven by large earthquakes on the Alpine fault, New Zealand. *Geology*, *40*(12), 1091–1094. https://doi.org/10.1130/G33486.1

Huang, M. Y.-F., & Montgomery, D. R. (2013). Altered regional sediment transport regime after a large typhoon, southern Taiwan. *Geology*, *41*(12), 1223–1226. https://doi.org/10.1130/G34826.1

Huber, A., Iroumé, A., Mohr, C., & Frêne, C. (2010). Effect of Pinus radiata and Eucalyptus globulus plantations on water resource in the Coastal Range of Biobio region, Chile. *Bosque (Valdivia)*, *31*(3), 219–230. https://doi.org/10.4067/S0717-92002010000300006

Jenson, S. K., & Domingue, J. O. (1988). Extracting topographic structure from digital elevation data for geographic information system analysis. *Photogrammetric Engineering and Remote Sensing*, *54*, 1593–1600. https://doi.org/0099-1112/88/5411-1593$02.25/0

Keefer, D. K. (1984). Landslides caused by earthquakes. *Geological Society of America Bulletin*, *95*(4), 406–421. https://doi.org/10.1130/0016-7606(1984)95<406:LCBE>2.0.CO

Keefer, D. K. (1994). The importance of earthquake-induced landslides to long-term slope erosion and slope-failure hazards in seismically active regions. *Geomorphology*, *10*(1–4), 265–284. https://doi.org/10.1016/0169-555X(94)90021-3

Khazai, B., & Sitar, N. (2004). Evaluation of factors controlling earthquake-induced landslides caused by Chi-Chi earthquake and comparison with the Northridge and Loma Prieta events. *Engineering Geology*, *71*(1–2), 79–95. https://doi.org/10.1016/S0013-7952(03)00127-3

Korup, O. (2005). Large landslides and their effect on sediment flux in South Westland, New Zealand. *Earth Surface Processes and Landforms*, *30*(3), 305–323. https://doi.org/10.1002/esp.1143

Korup, O. (2012). Earth's portfolio of extreme sediment transport events. *Earth-Science Reviews*, *112*(3–4), 115–125. https://doi.org/10.1016/j.earscirev.2012.02.006

Lacroix, P., Zavala, B., Berthier, E., & Audin, L. (2013). Supervised method of landslide inventory using panchromatic SPOT5 images and application to the earthquake-triggered landslides of Pisco (Peru, 2007, Mw8.0). *Remote Sensing*, *5*(6), 2590–2616. https://doi.org/10.3390/rs5062590

Ladson, A., Brown, R., Neal, B., & Nathan, R. (2013). A standard approach to baseflow separation using the Lyne and Hollick filter. *Australian Journal of Water Resources*, *17*(1). https://doi.org/10.7158/W12-028.2013.17.1

Larsen, I. J., Montgomery, D. R., & Korup, O. (2010). Landslide erosion controlled by hillslope material. *Nature Geoscience*, *3*(4), 247–251. https://doi.org/10.1038/ngeo776

Li, G., West, A. J., Densmore, A. L., Jin, Z., Parker, R. N., & Hilton, R. G. (2014). Seismic mountain building: Landslides associated with the 2008 Wenchuan earthquake in the context of a generalized model for earthquake volume balance. *Geochemistry, Geophysics, Geosystems*, *15*, 833–844. https://doi.org/10.1002/2013GC005067

Liaw, A., & Wiener, M. (2002). Classification and regression by randomForest. *R News*, *2*(3), 18–22. Retrieved from. https://cran.r-project.org/doc/Rnews/Rnews_2002-3.pdf

Lin, Y. N., Sladen, A., Ortega-Culaciati, F., Simons, M., Avouac, J.-P., Fielding, E. J., et al. (2013). Coseismic and postseismic slip associated with the 2010 Maule earthquake, Chile: Characterizing the Arauco Peninsula barrier effect. *Journal of Geophysical Research: Solid Earth*, *118*, 3142–3159. https://doi.org/10.1002/jgrb.50207

Major, J. J., Bertin, D., Pierson, T. C., Amigo, Á., Iroumé, A., Ulloa, H., & Castro, J. (2016). Extraordinary sediment delivery and rapid geomorphic response following the 2008-2009 eruption of Chaitén volcano, Chile. *Water Resources Research*, *52*, 5075–5094. https://doi.org/10.1002/2015WR018250

Maksaev, V., Munizaga, F., Zentilli, M., & Charrier, R. (2009). Fission track thermochronology of Neogene plutons in the Principal Andean Cordillera of central Chile (33-35°S): Implications for tectonic evolution and porphyry Cu-Mo mineralization. *Andean Geology*, *36*(2). https://doi.org/10.4067/S0718-71062009000200001

Malamud, B. D., Turcotte, D. L., Guzzetti, F., & Reichenbach, P. (2004). Landslides, earthquakes, and erosion. *Earth and Planetary Science Letters*, *229*(1–2), 45–59. https://doi.org/https://doi.org/10.1016/j.epsl.2004.10.018

Manga, M., & Wang, C.-Y. (2015). Earthquake hydrology. In *Treatise on Geophysics* (pp. 305–328). Elsevier. https://doi.org/10.1016/B978-0-444-53802-4.00082-8

Marc, O., Hovius, N., Meunier, P., Gorum, T., & Uchida, T. (2016). A seismologically consistent expression for the total area and volume of earthquake-triggered landsliding. *Journal of Geophysical Research: Earth Surface*, *121*, 640–663. https://doi.org/10.1002/2015JF003732

Marc, O., Hovius, N., Meunier, P., Uchida, T., & Hayashi, S. (2015). Transient changes of landslide rates after earthquakes. *Geology*, *43*(10), 883–886. https://doi.org/10.1130/G36961.1

Marc, O., Meunier, P., & Hovius, N. (2017). Prediction of the area affected by earthquake-induced landsliding based on seismological parameters. *Natural Hazards and Earth System Sciences*, *17*(7), 1159–1175. https://doi.org/10.5194/nhess-17-1159-2017

Melnick, D., Moreno, M., Quinteros, J., Baez, J. C., Deng, Z., Li, S., & Oncken, O. (2017). The super-interseismic phase of the megathrust earthquake cycle in Chile. *Geophysical Research Letters*, *44*, 784–791. https://doi.org/10.1002/2016GL071845

Meunier, P., Hovius, N., & Haines, J. A. (2008). Topographic site effects and the location of earthquake induced landslides. *Earth and Planetary Science Letters*, *275*(3–4), 221–232. https://doi.org/10.1016/j.epsl.2008.07.020

Miranda, A., Altamirano, A., Cayuela, L., AyLara, A., & González, M. (2017). Native forest loss in the Chilean biodiversity hotspot: Revealing the evidence. *Regional Environmental Change*, *17*(1), 285–297. https://doi.org/10.1007/s10113-016-1010-7

Mirus, B. B., Ebel, B. A., Mohr, C. H., & Zegre, N. (2017). Disturbance hydrology: Preparing for an increasingly disturbed future. *Water Resources Research*, *53*, 10,007–10,016. https://doi.org/10.1002/2017WR021084

Moernaut, J., Van Daele, M., Fontijn, K., Heirman, K., Kempf, P., Pino, M., et al. (2018). Larger earthquakes recur more periodically: New insights in the megathrust earthquake cycle from lacustrine turbidite records in south-central Chile. *Earth and Planetary Science Letters*, *481*, 9–19. https://doi.org/10.1016/j.epsl.2017.10.016

Moernaut, J., Van Daele, M., Strasser, M., Clare, M. A., Heirman, K., Viel, M., et al. (2015). Lacustrine turbidites produced by surficial slope sediment remobilization: A mechanism for continuous and sensitive turbidite paleoseismic records. *Marine Geology*, *384*, 159–176. https://doi.org/10.1016/j.margeo.2015.10.009

Mohr, C. H., Coppus, R., Iroumé, A., Huber, A., & Bronstert, A. (2013). Runoff generation and soil erosion processes after clear cutting. *Journal of Geophysical Research: Earth Surface*, *118*, 814–831. https://doi.org/10.1002/jgrf.20047

Mohr, C. H., Manga, M., Wang, C., Kirchner, J. W., & Bronstert, A. (2015). Shaking water out of soil. *Geology*, *43*(3), 207–210. https://doi.org/10.1130/G36261.1

Mohr, C. H., Manga, M., Wang, C. Y., & Korup, O. (2017). Regional changes in streamflow after a megathrust earthquake. *Earth and Planetary Science Letters*, *458*, 418–428. https://doi.org/10.1016/j.epsl.2016.11.013

Mohr, C. H., Montgomery, D. R., Huber, A., Bronstert, A., & Iroumé, A. (2012). Streamflow response in small upland catchments in the Chilean coastal range to the Mw 8.8 Maule earthquake on 27 February 2010. *Journal of Geophysical Research*, *117*(F2), F02032. https://doi.org/10.1029/2011JF002138

Mohr, C. H., Zimmermann, A., Korup, O., Iroumé, A., Francke, T., & Bronstert, A. (2014). Seasonal logging, process response, and geomorphic work. *Earth Surface Dynamics*, *2*(1), 117–125. https://doi.org/10.5194/esurf-2-117-2014

Montecinos, A., & Aceituno, P. (2003). Seasonality of the ENSO-related rainfall variability in central Chile and associated circulation anomalies. *Journal of Climate*, *16*(2), 281–296. https://doi.org/10.1175/1520-0442(2003)016<0281:SOTERR>2.0.CO;2

Montgomery, D. R., & Manga, M. (2003). Streamflow and water well responses to earthquakes. *Science*, *300*(5628), 2047–2049. https://doi.org/10.1126/science.1082980

Moreno, M., Melnick, D., Rosenau, M., Baez, J., Klotz, J., Oncken, O., et al. (2012). Toward understanding tectonic control on the Mw 8.8 2010 Maule Chile earthquake. *Earth and Planetary Science Letters*, *321-322*(0), 152–165. https://doi.org/10.1016/j.epsl.2012.01.006

Morera, S. B., Condom, T., Crave, A., Steer, P., & Guyot, J. L. (2017). The impact of extreme El Niño events on modern sediment transport along the western Peruvian Andes (1968-2012). *Scientific Reports*, *7*, 11947. https://doi.org/10.1038/s41598-017-12220-x

Moya, S., Sepúlveda, S., Serey, A., Montalva, G., Yugsi-Molina, F., Oróstegui, P., et al. (2015). Geomorphological and geotechnical analysis of landslides induced by the Maule earthquake 2010 in the Arauco Peninsula, Chile. In *XV Congreso Panamericano de Mecánica de suelos e Ingeniería Geotécnica* (pp. 3027–3033). Buenos Aires: IOS Press Ebooks. https://doi.org/10.3233/978-1-61499-603-3-3027

Moya, S., Sepúlveda, S. A., Serey, A., García, M., & Montalva, G. (2015). Remociones en masa generadas por el terremoto del Maule de 2010 en la Península de Arauco. In *XIV Congreso Geológico Chileno* (pp. 19–22). Coquimbo.

Natahan, R. J., & McMahon, T. A. (1990). Evaluation of automated techniques for baseflow and recession analyses. *Water Resources Research*, *26*(7), 1465–1473. https://doi.org/10.1029/90WR00136

Pritchard, M. E., Jay, J. A., Aron, F., Henderson, S. T., & Lara, L. E. (2013). Subsidence at southern Andes volcanoes induced by the 2010 Maule, Chile earthquake. *Nature Geoscience*, *6*(8), 632–636. https://doi.org/10.1038/ngeo1855

R Core Team. (2018). R: A Language and Environment for Statistical Computing. Vienna, Austria. Retrieved from https://www.r-project.org/

Roback, K., Clark, M. K., West, A. J., Zekkos, D., Li, G., Gallen, S. F., et al. (2018). The size, distribution, and mobility of landslides caused by the 2015 Mw7.8 Gorkha earthquake, Nepal. *Geomorphology*, *301*, 121–138. https://doi.org/10.1016/j.geomorph.2017.01.030

Rodríguez, C. E., Bommer, J. J., & Chandler, R. J. (1999). Earthquake-induced landslides: 1980-1997. *Soil Dynamics and Earthquake Engineering*, *18*(5), 325–346. https://doi.org/10.1016/S0267-7261(99)00012-3

Rodríguez-Echeverry, J., Echeverría, C., Oyarzún, C., & Morales, L. (2018). Impact of land-use change on biodiversity and ecosystem services in the Chilean temperate forests. *Landscape Ecology*, *33*(3), 439–453. https://doi.org/10.1007/s10980-018-0612-5

Saragoni, S., & Ruiz, S. (2012). Implicaciones y nuevos desafíos de diseño sísmico de los acelerogramas del terremoto de 2010. In *M_w=8.8 Terremoto en Chile. 27 de febrero de 2010* (pp. 127–146). Santiago de Chile: Departamento Ingeniería Civil, Universidad de Chile.

Schuller, P., Walling, D. E., Iroumé, A., Quilodrán, C., Castillo, A., & Navas, A. (2013). Using 137Cs and 210Pbex and other sediment source fingerprints to document suspended sediment sources in small forested catchments in south-central Chile. *Journal of Environmental Radioactivity*, *124*, 147–159. https://doi.org/10.1016/j.jenvrad.2013.05.002

Sepúlveda, S. A., Moreiras, S., Lara, M., & Alfaro, A. (2015). Debris flows in the Andean ranges of central Chile and Argentina triggered by 2013 summer storms: Characteristics and consequences. *Landslides*, *12*(1), 115–133. https://doi.org/10.1007/s10346-014-0539-0

Sepúlveda, S. A., Murphy, W., & Petley, D. N. (2005). Topographic controls on coseismic rock slides during the 1999 Chi-Chi earthquake, Taiwan. *Quarterly Journal of Engineering Geology and Hydrogeology*, *38*(2), 189–196. https://doi.org/10.1144/1470-9236/04-062

Sepúlveda, S. A., Serey, A., Lara, M., Pavez, A., & Rebolledo, S. (2010). Landslides induced by the April 2007 Aysén fjord earthquake, Chilean Patagonia. *Landslides*, *7*(4), 483–492. https://doi.org/10.1007/s10346-010-0203-2

Serey, A., Escobar, P., Moya, S., Sepúlveda, S. A., & Petley, D. N. (2017). Landslide inventory of the 2010 Mw 8.8 Maule earthquake, Central Chile. In *16th World Conference on Earthquake Engineering*. Santiago, Chile.

Serey, A., Piñero-Feliciangeli, L., Sepúlveda, S. A., Poblete, F., Petley, D. N., & Murphy, W. (2019). Landslides induced by the 2010 Chile megathrust earthquake: A comprehensive inventory and correlations with geological and seismic factors. *Landslides*. https://doi.org/10.1007/s10346-019-01150-6

Sernageomin (2003). Mapa geológico de chile: Version digital. *Publicacion Geologia Digital*. Retrieved from http://geoportal.sernageomin.cl/geovisor/GeoVisor/index.html?resources=map:ags@http://geoarcgis.sernageomin.cl/ArcGIS/rest/services/geoportal/GeologiaBase/MapServer

Shi, Z., Wang, G., Manga, M., & Wang, C.-Y. (2015). Continental-scale water-level response to a large earthquake. *Geofluids*, *15*(1–2), 310–320. https://doi.org/10.1111/gfl.12099

Sidle, R. C., & Ochiai, H. (2006). *Landslides: Processes, prediction, and land use* (Vol. 18). Washington, DC: American Geophysical Union. https://doi.org/10.1029/WM018

Solar, W. (1999). Manual de terreno y centros de filtrado. Centro de Información Recursos Hídricos, Dirección General de Aguas, Gobierno de Chile. Retrieved from http://documentos.dga.cl/SED4939.pdf

Soto, L., Galleguillos, M., Seguel, O., Sotomayor, B., & Lara, A. (2019). Assessment of soil physical properties' statuses under different land covers within a landscape dominated by exotic industrial tree plantations in south-central Chile. *Journal of Soil and Water Conservation*, *74*(1), 12–23. https://doi.org/10.2489/jswc.74.1.12

Spikings, R., Dungan, M., Foeken, J., Carter, A., Page, L., & Stuart, F. (2008). Tectonic response of the central Chilean margin (35–38gradS) to the collision and subduction of heterogeneous oceanic crust: a thermochronological study. *Journal of the Geological Society*, *165*(5), 941–953. https://doi.org/10.1144/0016-76492007-115

Strobl, C., Boulesteix, A. L., Kneib, T., Augustin, T., & Zeileis, A. (2008). Conditional variable importance for random forests. *BMC Bioinformatics*, *9*(1), 1–11. https://doi.org/10.1186/1471-2105-9-307

Tapia, F., Farías, M., Naipauer, M., & Puratich, J. (2015). Late Cenozoic contractional evolution of the current arc-volcanic region along the southern Central Andes (35°20′S). *Journal of Geodynamics*, *88*, 36–51. https://doi.org/10.1016/j.jog.2015.01.001

Tarboton, D. G. (1997). A new method for the determination of flow directions and upslope areas in grid digital elevation models. *Water Resources Research*, *33*(2), 309–319. https://doi.org/10.1029/96WR03137

Tolorza, V., Carretier, S., Andermann, C., Ortega-Culaciati, F., Pinto, L., & Mardones, M. (2014). Contrasting mountain and piedmont dynamics of sediment discharge associated with groundwater storage variation in the Biobío river. *Journal of Geophysical Research: Earth Surface*, *119*, 2730–2753. https://doi.org/10.1002/2014JF003105

USGS (2010). Shakemap archive. Retrieved December 20, 2015, from https://earthquake.usgs.gov/earthquakes/eventpage/official20100227063411530_30#shakemap

Van Daele, M., Moernaut, J., Doom, L., Boes, E., Fontijn, K., Heirman, K., et al. (2015). A comparison of the sedimentary records of the 1960 and 2010 great Chilean earthquakes in 17 lakes: Implications for quantitative lacustrine palaeoseismology. *Sedimentology*, *62*(5), 1466–1496. https://doi.org/10.1111/sed.12193

Viale, M., & Garreaud, R. (2014). Summer precipitation events over the western slope of the subtropical Andes. *Monthly Weather Review*, *142*(3), 1074–1092. https://doi.org/10.1175/MWR-D-13-00259.1

Vigny, C., Socquet, A., Peyrat, S., Ruegg, J.-C., Métois, M., Madariaga, R., et al. (2011). The 2010 Mw 8.8 Maule megathrust earthquake of Central Chile, monitored by GPS. *Science*, *332*(6036), 1417–1421. https://doi.org/10.1126/science.1204132

Vorpahl, P., Dislich, C., Elsenbeer, H., Märker, M., & Schröder, B. (2013). Biotic controls on shallow translational landslides. *Earth Surface Processes and Landforms*, *38*(2), 198–212. https://doi.org/10.1002/esp.3320

Wagenbrenner, J. W., & Robichaud, P. R. (2014). Post-fire bedload sediment delivery across spatial scales in the interior western United States. *Earth Surface Processes and Landforms*, *39*(7), 865–876. https://doi.org/10.1002/esp.3488

Wang, C. Y., & Manga, M. (2011). Hydrologic Responses to Earthquakes and a General Metric. *Frontiers in Geofluids*, 206–216. https://doi.org/10.1002/9781444394900.ch14

Wang, J., Jin, Z., Hilton, R. G., Zhang, F., Densmore, A. L., Li, G., & West, A. J. (2015). Controls on fluvial evacuation of sediment from earthquake-triggered landslides. *Geology*, *43*(2), 115–118. https://doi.org/10.1130/G36157.1

Wartman, J., Dunham, L., Tiwari, B., & Pradel, D. (2013). Landslides in Eastern Honshu induced by the 2011 Tohoku earthquake. *Bulletin of the Seismological Society of America*, *103*(2B), 1503–1521. https://doi.org/10.1785/0120120128

Wessel, P., Smith, W. H. F., Scharroo, R., Luis, J., & Wobbe, F. (2013). Generic mapping tools: Improved version released. *Eos, Transactions American Geophysical Union*, *94*(45), 409–410. https://doi.org/10.1002/2013EO450001

Zhao, Y., Feng, D., Yu, L., Wang, X., Chen, Y., Bai, Y., et al. (2016). Detailed dynamic land cover mapping of Chile: Accuracy improvement by integrating multi-temporal data. *Remote Sensing of Environment*, *183*, 170–185. https://doi.org/10.1016/j.rse.2016.05.016